

# Feasibility Study for Measuring Geomagnetic Conversion of Solar Axions to X-rays in Low Earth Orbits

Hooman Davoudiasl\*

*Department of Physics, Brookhaven National Laboratory, Upton, NY 11973, USA*

Patrick Huber†

*Physics Department, Theory Division,*

*CERN, 1211 Geneva 23, Switzerland and*

*Department of Physics, Virginia Tech, Blacksburg, VA 24062, USA*

(Dated: November 7, 2018)

We present a detailed computation of the expected rate for Geomagnetic Conversion of Solar Axions to X-rays (GECOSAX) along the orbit of an x-ray satellite. We use realistic satellite orbits and propagation in time. A realistic model for the Earth's magnetic field, which properly accounts for its spatial non-uniformity, is used. We also account for the effect of the Earth's atmosphere on the propagation of x-rays in our calculation of axion-photon conversion probability. To estimate possible sensitivities to the axion-photon coupling  $g_{a\gamma}$ , we use an actual measurement of the expected backgrounds by the SUZAKU satellite. Assuming a detector area of  $10^3 \text{ cm}^2$  and about  $10^6 \text{ s}$  of data, we show that a  $2\sigma$  limit of  $g_{a\gamma} < (4.7 - 6.6) \times 10^{-11} \text{ GeV}^{-1}$  from GECOSAX is achievable, for axion masses  $m_a < 10^{-4} \text{ eV}$ . This significantly exceeds current laboratory sensitivities to  $g_{a\gamma}$ .

## I. INTRODUCTION

Weakly interacting light pseudo-scalars are well-motivated in particle physics. For example, experimental observations require the size of  $CP$  violation in strong interactions, parametrized by the angle  $\theta$ , to be quite small:  $\theta \lesssim 10^{-10}$ . However, the symmetries of the

---

\*Electronic address: hooman@bnl.gov

†Electronic address: pahuber@vt.edu

Standard Model (SM) allow  $\theta \sim 1$ ; this is the strong  $CP$  problem. An elegant solution to this puzzle was proposed by Peccei and Quinn (PQ) [1, 2], where a new  $U(1)$  symmetry, anomalous under strong interactions, was proposed. This  $U(1)$  symmetry is assumed to be spontaneously broken at a scale  $f_a$ , resulting in a pseudo-scalar Goldstone boson  $a$  [3, 4], the axion. Non-perturbative QCD interactions at the scale  $\Lambda_{\text{QCD}} \sim 100 \text{ MeV}$  generate a potential and hence a mass  $m_a^{PQ} \sim \Lambda_{\text{QCD}}^2/f_a$  for the axion. Experimental and observational bounds have pushed  $f_a$  to scales of order  $10^7 \text{ GeV}$  or more. As  $f_a$  sets the inverse coupling of the axion to the SM fields, the current data suggests that axions are basically ‘invisible’ and very light. Here we note that some cosmological considerations related to the overclosure of the universe suggest an upper bound  $f_a \lesssim 10^{12} \text{ GeV}$  for the PQ axion [5, 6, 7, 8]. Apart from the considerations related to the strong  $CP$  problem, axion-like particles are ubiquitous in string theory. In addition, axion-like particles have been used in various astrophysical and cosmological models<sup>1</sup>. In the following, the term axion is generically used to refer to any of the above, or other, possible instances of such weakly interacting light pseudo-scalars.

The coupling of the axion to photons is given by [10]

$$\mathcal{L}_{a\gamma} = -\frac{a}{4M} F_{\mu\nu} \tilde{F}^{\mu\nu} = g_{a\gamma} a \vec{E} \cdot \vec{B}, \quad (1)$$

where  $M \sim (\pi/\alpha)f_a$  and  $\alpha \simeq 1/137$  is the fine structure constant.  $F_{\mu\nu}$  is the electromagnetic field strength tensor,  $\tilde{F}^{\mu\nu}$  is its dual,  $g_{a\gamma} \equiv M^{-1}$  is the axion-photon coupling;  $\vec{E}$  and  $\vec{B}$  are the electric and magnetic fields, respectively, corresponding to  $F_{\mu\nu}$ . The interaction in (1) makes it possible for hot plasmas, like the Sun, to emit a flux of axions through the Primakoff process [11]. This same interaction has also led to experimental proposals [12] for detecting the axion through its conversion to photons in external magnetic fields. Various experimental bounds, most recent of which is set by the CAST experiment [13], suggest that  $g_{a\gamma} \lesssim 10^{-10} \text{ GeV}^{-1}$ . For a review of different bounds on axion couplings, see Ref. [14].

In what follows, we study the feasibility of a recently proposed approach for detecting solar axions with an x-ray telescope in orbit [15], based on geomagnetic conversion of solar axions to x-rays (GECOSAX)<sup>2</sup>. The estimate of the expected x-ray flux presented in Ref. [15] was based on a number of simplifying assumptions:

---

<sup>1</sup> See, for example, Ref. [9].

<sup>2</sup> The possibility of using planetary magnetic fields as a conversion region for high energy cosmic axions was discussed in Ref. [16].

1. The satellite orbit was a circle.
2. The orbit was aligned to lie in the equatorial plane of the Earth.
3. The Earth axis was perpendicular to the Ecliptic.
4. The available conversion length was taken to be the altitude of the satellite.
5. The magnetic field was assumed uniform and perpendicular to the direction of axion propagation.
6. The effect of the Earth atmosphere was neglected. Consequently, the effective mass of the photon in medium was ignored;  $m_\gamma \rightarrow 0$ .

These assumptions allowed a treatment of GECOSAX within the same formalism relevant for helioscopes [12, 17], *i.e.* axion-photon conversion *in vacuo* in a constant magnetic field which is perpendicular to the direction of the axion momentum. The conversion rate, in the limit of vanishing axion mass  $m_a \rightarrow 0$ , is then simply given by

$$P_{a\gamma}^s = 2.45 \times 10^{-21} \left( \frac{g_{a\gamma}}{10^{-10} \text{ GeV}^{-1}} \right)^2 \left( \frac{B}{\text{T}} \right)^2 \left( \frac{L}{\text{m}} \right)^2. \quad (2)$$

Taking  $g_{a\gamma} = 10^{-10} \text{ GeV}^{-1}$  and using CAST parameters  $B = 9 \text{ T}$  and  $L = 10 \text{ m}$ , we obtain  $P_{a\gamma}^s \simeq 2 \times 10^{-17}$ . Replacing the CAST magnet with the geomagnetic field and taking  $L$  to characterize a low-Earth-orbit, we have  $B = 3 \times 10^{-5} \text{ T}$  and  $L = 6 \times 10^5 \text{ m}$  and thus get for  $P_{a\gamma}^s \simeq 8 \times 10^{-19}$ , which is only a factor of about 25 smaller than the CAST conversion probability. However, in Ref. [15], it was noted that this can typically be overcompensated by the larger detection area of an orbiting x-ray telescope. In [15] it was shown that the resulting x-ray signal on the dark side of the Earth would have a number of unique features which would make it very hard to be mistaken for anything else: upward going x-rays,  $T = 4 \text{ keV}$  black body spectrum, direction from within  $3'$  from the center of the Sun and characteristic modulation with  $B^2 L^2$ .

In the following, we would like to address the simplifying assumptions one by one and illustrate their effect on the actual axion-photon conversion rate. In section II, we will discuss how to account for the proper satellite-Sun-Earth geometry. We will also discuss how to compute the actual position of any given satellite. This will address assumptions 1-4. Next we will address assumption 5 in section III with a proper magnetic model. In

section IV, we will present a full treatment of axion-photon conversion in a dispersive and absorptive medium, using a model of the Earth’s atmosphere, which addresses assumption 6. In section V, we will present the resulting x-ray fluxes for various satellites, followed by a discussion of achievable sensitivities for  $g_{a\gamma}$ , in section VI. Finally, we will present a discussion of our results and the future outlook, in section VII.

## II. GEOMETRY AND SATELLITE ORBITS

The basis for any detailed calculation of the axion-photon conversion rate is a correct description of the geometry. We introduce the following notation: plain capital Latin or Greek letters denote a point, where  $O$  denotes the origin of our coordinate system. If  $P$  is a point, then its position vector  $\overline{OP}$  is denoted by  $\vec{p}$ . For any vector  $\vec{v}$  its length is denoted by  $v$ . The unit vector along the direction of  $\vec{v}$  is denoted by  $\vec{e}_v = \vec{v}/v$ . The Sun is at  $S$ , the center of the Earth is at  $E$  and the x-ray satellite is at  $X$ . For any point  $P$ , we define its height vector  $\vec{h}_P$  as the vector which goes from the surface of the Earth to  $P$  and is perpendicular to the tangent plane of the Earth surface at its starting point. The starting point is called the footprint of  $P$  and denoted by  $P_F$ . This definition may seem involved, however, it also holds for the actual geoid and not only for a spherical Earth.

The abstract definition of the problem can be easily done without specifying a coordinate system. The actual numerical calculation, of course, has to specify a definite coordinate system, which is relegated to appendix A.

In Fig. 1 a two dimensional schematic view of the problem is shown at one instant in time  $t_0$ . Since axions/photons travel close to/at the speed of light  $c$ , they experience an essentially static environment. The geometry only changes notably on timescales large compared to the propagation time  $\tau_p \sim 10^6 \text{ m}/c \sim 10^{-3} \text{ s}$ . Therefore, the geometry can be regarded as fixed at any given time  $t_0$ . The first task is to determine the path traveled by the axions. The axions propagate in a straight line from the Sun  $S$  to the satellite  $X$ . For axion conversion, however, only the part of  $\overline{SX}$  which is on the dark side of the Earth is relevant. Thus, the intersections of  $\overline{SX}$  with the surface of the Earth have to be found. We account for the ellipsoidal shape of the Earth and use the so called WGS72 parameters<sup>3</sup>. In general there can be none, one or

---

<sup>3</sup> For polar orbits the difference in radius of a spherical and ellipsoidal Earth can cause up to a 10 s difference in the duration of the dark orbit.

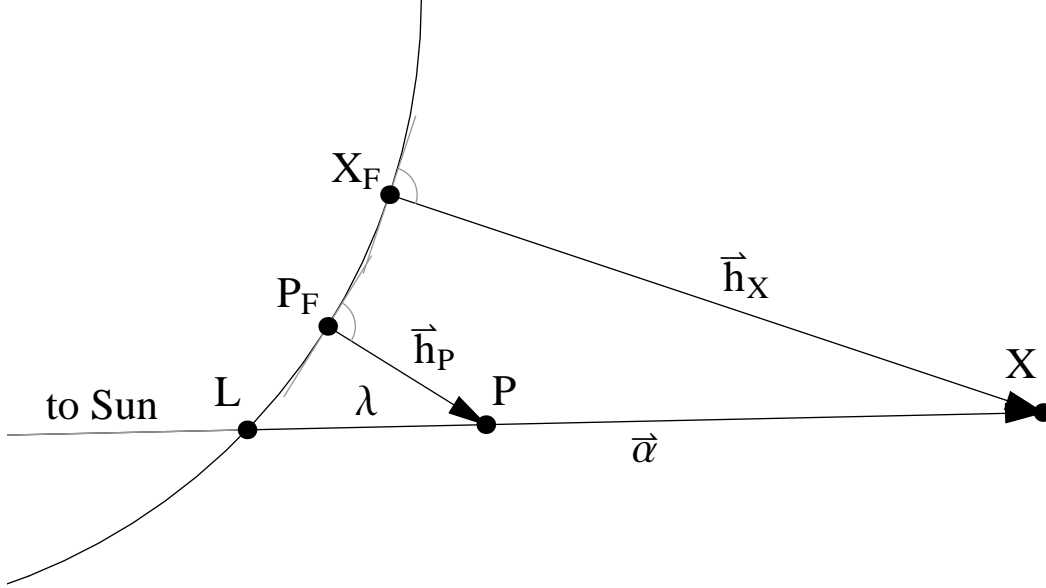


FIG. 1: Geometry of the GECOSAX configuration drawn in the plane spanned by the center of the Earth, the center of the Sun and the satellite's position at  $t_0$ .

two such intersections. The solution on the dark side will be denoted by  $L$ . This allows us to define the line of sight (LOS)  $\vec{a} = \overline{LX}$ . Note, that this definition of being on the dark side is purely geometrical and neglects the angular diameter of the Sun, atmospheric refraction and absorption. The angular diameter of the Sun reduces the useful part of the orbit by about 4s. This follows from the fact that the Sun subtends  $0.5^\circ$  and the satellite travels a full circle in about 90 minutes. The effect of the Earth atmosphere is quite a bit larger since it becomes non-transparent for x-rays below an altitude of about 50 – 100 km, thus increasing the effective radius by that amount, which by explicit calculation would increase the dark orbit duration by a few times 10s. This overcompensates for our neglect of the solar diameter and makes our overall treatment conservative. Using the position of  $L$  as defined above, one can parametrize the position of any point along the line of sight

$$\vec{p}(\lambda) \equiv \lambda \vec{e}_\alpha + \vec{l}. \quad (3)$$

In the course of the actual calculation the height  $h_P$  of  $P$  is needed, since the air density is a function of the actual height. Note that the height of the satellite  $h_X$  is always smaller than the length of the LOS, *i.e.*  $h_X \leq \alpha$ . This implies that assumption 4 is in fact conservative, and we will find that the relative increase of  $\alpha$  with respect to  $h_X$  will compensate largely for

the losses in x-ray flux due to the other effects considered in the following. The algorithm for the solar position is taken from [18] and its accuracy is better than 1'.

The idealized orbit of any satellite is a solution to the Kepler problem. Thus, knowing the satellite's position and velocity at time  $t_0$ , it is possible to predict its future position at  $t_1$ . In reality, there are, however, various factors which lead to deviations from the simple Kepler orbit, among which are: non-vanishing higher multipoles of the mass distribution of the Earth, atmospheric drag, gravitational influence from the Moon (and to a lesser degree from the Sun), *etc.*. The prediction of satellite orbits is, of course, a matter of great importance for operators of satellites and is also needed for military applications. The aforementioned effects disturbing the simple Kepler orbit can be accounted for in a general<sup>4</sup> perturbation theory. Many of the perturbations are well known and can be quite exactly computed. From the observation of the actual position and velocity of a satellite at time  $t_0$  it is possible to extract the unperturbed Kepler orbit, which would follow in the absence of any perturbing factors. In order to obtain an accurate prediction for the future, a specific set of perturbations is taken into account. In doing this, it is crucial that the initial unperturbed Keplerian orbit data is extracted using a model which is compatible with the algorithm used for future positions.

One standard format is the so called 'NORAD<sup>5</sup> element sets', and a description of the perturbation model called SGP4<sup>6</sup> can be found in [19]. Since satellite propagation is done in perturbation theory, errors inevitably will accumulate and render the predictions unreliable. Therefore, element sets for basically all active satellites are issued periodically by NORAD and made accessible at [20] in the so called 'two line element' (TLE) format. The implementation of the NORAD orbit prediction algorithm we use is taken from the `predict` program, which is an open-source C language satellite tracking software [21]<sup>7</sup>. It directly

---

<sup>4</sup> General in the sense, that the resulting theory is applicable to a wide, general class of orbits and not restricted to particular orbits like *e.g.* ones with a low eccentricity.

<sup>5</sup> NORAD is the North American Aerospace Defense Command.

<sup>6</sup> SGP4 stands for 'simplified general perturbation version 4'. Historically, one distinguished SGP4 and SDP4, where the latter one is used for 'deep-space' orbits with periods longer than 225 minutes. For most parts of this work, we use only SGP4, *i.e.* orbits with periods smaller than 225 minutes.

<sup>7</sup> In reality, it seems that all implementations found in open accessible sources go back to various, different original implementations by T.S Kelso [20] in a number of programming languages. The one we are using is no exception.

takes the TLE of a satellite, a time  $t_0$  and returns its position in the ECI<sup>8</sup> at  $t_0$ . All satellites are indexed by NORAD using so called US SPACECOM identification numbers, these are 5 digit numbers starting with 00001 for the SPUTNIK satellite. We will use these 5 digit numbers to refer to all satellites in this paper, any satellite names are written in capitals. A list of all US SPACECOM IDs and the corresponding names is given in table III.

Some remarks about our use of TLEs and SGP4 are in order. We use SGP4 since it is the simplest general purpose algorithm and the necessary input data, the TLEs, are easily available. SGP4 is by no means state of the art, it was developed to allow reliable tracking of thousands of objects with the limited computing power available in the 60s and 70s. Clearly, in an actual experiment one would use telemetry data and direct numerical integration, possibly even GPS, thus reducing any position errors to around 100 m or less [22]. The accuracy of predictions made with SGP4 relative to GPS position determination was studied in detail in [22]. The typical errors for SGP4 are about  $\pm 5$  km cross-track, *i.e.* perpendicular to the satellite momentum, within  $\pm 15$  days from the epoch of the used TLE, whereas the in-track error, *i.e.* along the orbit, is about  $\pm 20$  km. For a satellite moving at about 10 km/s this gives rise to a timing error of about 2 s. We checked that these errors have, in fact, a very small impact on the average axion signal, since the satellite still reaches every point under more or less the same circumstance with respect to magnetic field orientation and direction to the Sun. For this test, we used historic TLEs of satellite 27370 (RHESSI), obtained from [20], issued about 8 months apart. We found that there was a time difference of several minutes in when the satellite entered the dark orbit, but once we corrected for this time shift, the GECOSAX fluxes were identical to within  $\sim 10\%$ . In [22] it is shown that the inter-TLE variation is a good indicator for the actual accuracy. This is clearly an extreme example since TLEs are re-issued about every other week. Thus, we conclude that SGP4 with current TLEs is accurate enough by a large margin.

To summarize, we found that the corrections due to the proper treatment of the geometry are quite large and lead to a pronounced variation of the expected flux along each orbit because of changes in the length  $\alpha$  of the LOS. Geometry related effects are accounted within about  $\pm 25$  km or  $\pm 5$  s in our calculation, which introduces less than 10% error in the GECOSAX signal prediction. The errors introduced by our simplified treatment of

---

<sup>8</sup> This is an Earth Centered Inertial set of coordinates, discussed in appendix A.

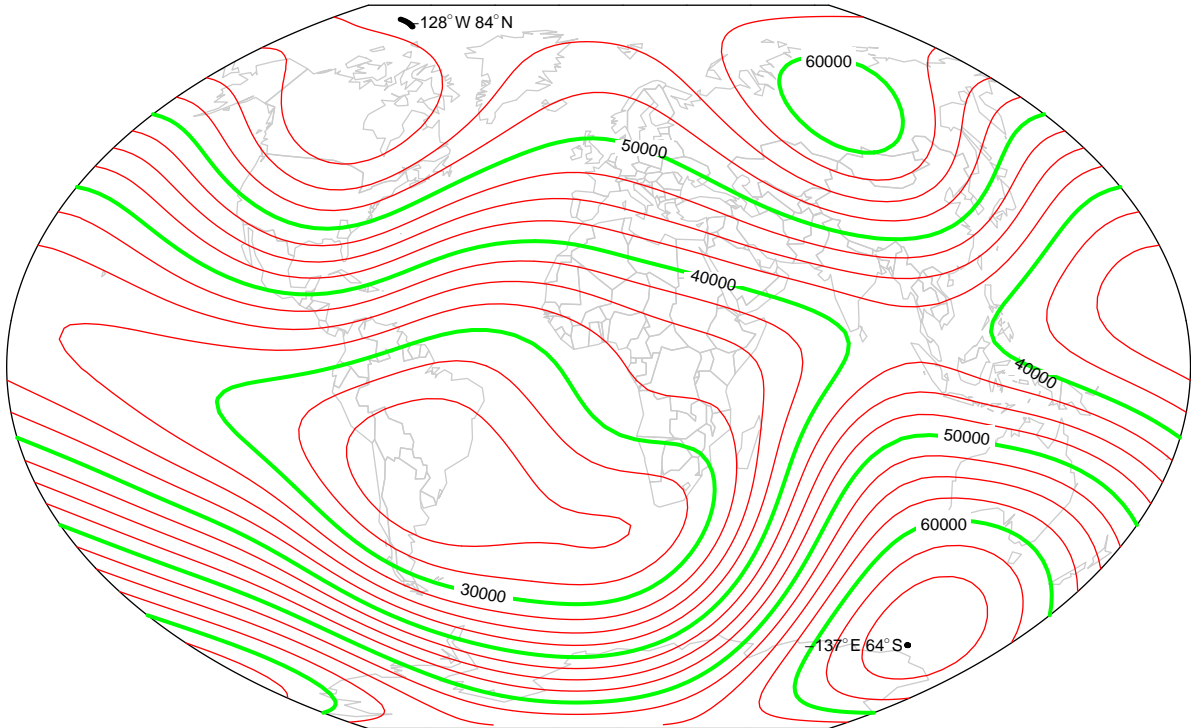


FIG. 2: Map of the total magnetic field strength at sea level for 2008.5 [23]. Red, thick contours are in steps of 10 000 nT, thin red ones are in steps of 2 500 nT. The number on top of the red, thick contours are the magnetic field strength in nT. The black dots denote the positions of the magnetic dip pole for each year from 2005 till 2010. The coordinates give the position of the dip pole in 2008.5. The map is a Winkel tripel projection.

coordinate transformation in appendix A are negligible in comparison to the intrinsic errors of the satellite orbit prediction.

### III. MAGNETIC FIELD OF THE EARTH

To a first approximation, the magnetic field of the Earth is a dipole whose axis intersects the surface at the magnetic poles, which do not coincide with the geographic ones. This mis-alignment of rotation and magnetic axes alone would induce a typical periodic variation of the x-ray flux produced by GECOSAX. However, the geomagnetic field has various other irregularities and deviations from a simple dipole form.

We use a realistic 3-d model of the magnetic field of the earth, the so called World Magnetic Model 2005 [24], which is available in machine readable form at [23]. The World



Magnetic Model is the standard model of the US Department of Defense, the UK Ministry of Defense, the North Atlantic Treaty Organization (NATO), and the World Hydrographic Office (WHO) for navigation and attitude/heading referencing systems. It is intended to meet its stringent error specifications (better than 1%) from sea level up to an altitude of 600 km. Since it is given as a series expansion in spherical harmonics, mathematically it stays well-defined out to larger radii. If there were no electrical currents in the upper atmosphere and no solar wind, *i.e.* additional sources of magnetic fields outside the Earth, the model would be accurate up to many Earth radii. In practice, interactions with the solar wind and atmospheric electrical currents produce magnetic fields of around 100 – 500 nT, at an altitude of  $\sim 1000$  km, during magnetically quiet times and perturbations can reach up 2000 nT during strong magnetic storms. Magnetic perturbations are indexed by the  $A_p$  index, which is the daily average of the  $a_p$  index. It denotes the deviation from the most disturbed component of the local magnetic field vector from its mean, undisturbed value in units of 2 nT. The  $A_p$  index is derived from the observations of 11 geomagnetic observatories and has been regularly collected since 1932.  $A_p$  values larger than 100 are classified as indicating a severe magnetic storm. Only 1% of the days from 1932 till 1992 have reported a value of  $A_p > 100$  [25]. Hence, for almost all observation conditions the errors introduced by the day to day variability of the geomagnetic field will be small. Thus, the errors introduced by using the magnetic model up to an altitude of 1000 km are certainly less than 10%, most likely much less than 5% [26, 27, 28]. Therefore, in principle, it seems feasible to extend the permissible range of altitudes maybe up to 1-2 Earth radii, however, this would require a more careful analysis of the external magnetic fields, which is beyond the scope of this work. We, therefore, will restrict all analysis to altitudes below 1 000 km, unless otherwise mentioned.

The magnetic model also includes a prediction of the annual variation of geomagnetic parameters from 2005 to 2010. From these variations we expect a less than 1% annual change in the relevant parameters. Given this 3-d vectorial map, we compute the transverse  $\vec{B}$ -field along the axion path. The total field strength is shown in Fig. 2.

#### IV. AXION PROPAGATION

The axions and x-rays will have to traverse the upper Earth atmosphere, which causes absorption and refraction of x-rays and hence will also influence the axion-photon conversion probability. To a rough approximation the interaction of x-rays with an energy of few keV with air can be described by Thomson scattering from free electrons [29]. Air mostly consists of nitrogen and oxygen having atomic numbers  $Z$  of 7 and 8, respectively. The binding energies of the innermost electrons thus are about  $Z^2 13.6 \text{ eV} \simeq 600 - 800 \text{ eV}$  and thus small compared to the photon energy for most of the range of interest. On the other hand, the photon energies are very small compared to the rest mass of the electron and hence the scattering is highly non-relativistic and pair creation cannot take place. Thus, all effects on x-ray propagation should be a function of the electron density, which itself closely traces the mass density of air. At standard temperature and pressure (STP) of 273.15 K and 101 325 Pa, we use as volume (molar) fractions 78.1% N<sub>2</sub>, 21.0% O<sub>2</sub>, and 0.93% Ar<sup>9</sup>.

The absorption length  $\lambda = \Gamma^{-1}$  for x-rays of energy 1 – 10 keV, in air at STP, has been obtained from [29, 30]. We have assumed that x-ray absorption scales with the electron density along the axion path. Assuming a constant composition of the atmosphere with altitude, the electron density<sup>10</sup> is directly proportional to the mass density.

To include refraction, we use the effective photon mass  $m_\gamma$  given by [17]

$$m_\gamma^2 = 4\pi r_0 [\rho f_1 / (A m_u)], \quad (4)$$

where  $r_0 \simeq 2.82 \times 10^{-15} \text{ m}$  is the classical electron radius,  $A$  is the atomic mass number of the gas (atmosphere),  $m_u$  is the atomic mass unit,  $\rho$  is the gas density,  $f_1 \simeq Z$ , and  $Z$  is atomic number of the gas. This formula can be generalized for a compound gas, like the air, by noting that the quantity  $\rho Z / (A m_u)$  is the electron number density  $n_e$  for the medium, which in the above equation is assumed to be made up of only one element.

For a simplified derivation we assume that air is composed of 78% N<sub>2</sub> and 22% O<sub>2</sub>, by volume. In the ideal gas limit, the volume and molar fractions are the same. Given that for dry air the molar density is  $\rho_{air} \simeq 44.48 \text{ mol m}^{-3}$  (STP), we find that  $n_e \simeq$

---

<sup>9</sup> With  $Z = 18$ , Ar has binding energies in the keV range. However, due to its small molar fraction we may ignore it for the exposition, here. In the numerical analysis it is accounted for.

<sup>10</sup> We will comment on this in more detail, later in this section.

$44.48 N_A(0.78 \times 14 + 0.22 \times 16) \simeq 3.87 \times 10^{26} \text{ m}^{-3}$ , where  $N_A$  is Avogadro's number. Then, Eq. (4) yields

$$m_\gamma = 0.64 \left( \frac{\rho}{\text{kg m}^{-3}} \right)^{1/2} \text{ eV}. \quad (5)$$

We checked that using the full energy dependence of  $f_1$  given in [29, 30] and a more detailed air composition does not change  $m_\gamma$  by more than 2%.

As the following general argument will show, the axion conversion path length is only logarithmically sensitive to density variations. In all density models, the density profile can be locally described by an exponential with an altitude dependent scale height  $H(h)$

$$\rho(h) \equiv \rho_0 e^{-\frac{h}{H(h)}}, \quad (6)$$

where both  $\rho_0$  and  $H(h)$  can be time dependent. In order to estimate the impact on axion propagation, we need to understand up to what altitude absorption plays a role and what impact a finite photon mass has. In order to asses the sensitivity to changes in absorption we can compute the escape probability  $p_{\text{esc}}$  of a x-ray photon from a given altitude  $\eta$  to infinity:

$$p_{\text{esc}} = e^{-c_p} \quad \text{with} \quad c_p = \int_{\eta}^{\infty} dx \Gamma(x), \quad (7)$$

where  $\Gamma(x)$  is the inverse absorption length and  $c_p$  the so called absorption coefficient.  $\Gamma(x)$  itself is a function of the density and is given by

$$\Gamma(x) \equiv \mu \rho(x), \quad (8)$$

where  $\mu$  is the mass attenuation coefficient. We now can define the escape altitude  $a_{\text{esc}}$  by demanding  $p_{\text{esc}} = 1/e$ . This then translates to the following condition

$$1 \stackrel{!}{=} c_p = \int_{\eta_{\text{esc}}}^{\infty} dx \Gamma(x) = \int_{\eta_{\text{esc}}}^{\infty} dx \mu \rho_0 e^{-\frac{x}{H(x)}}. \quad (9)$$

Assuming that  $H(x) = H = \text{const.}$  we can easily solve for  $x$  and obtain

$$\eta_{\text{esc}} = H \ln(H \rho_0 \mu). \quad (10)$$

The effect of a non-vanishing  $m_\gamma$  is the same as the one of a non-vanishing axion mass: they both affect the oscillation or coherence length for photon-axion conversion. The conversion probability will be suppressed whenever the oscillation length is short compared to

the available path length. For the following discussion we define the oscillation length  $l_\gamma$  to be due to the finite photon mass

$$l_\gamma = \frac{4\pi\omega}{m_\gamma^2}, \quad (11)$$

where  $\omega$  denotes the photon energy. In order for  $m_\gamma$  to be negligible, we require  $l_\gamma < L \simeq 1000$  km. Since  $m_\gamma \propto \sqrt{\rho}$ , it follows that  $l_\gamma \propto \rho^{-1}$ . The altitude  $\eta$  at which  $l_\gamma$  reaches a certain value can be computed, using Eqs. 5 and 6

$$\eta = H \ln \left[ 1.65 \times 10^5 \left( \frac{l_\gamma}{\text{km}} \right) \left( \frac{\rho_0}{\text{kg m}^{-3}} \right) \left( \frac{\text{keV}}{\omega} \right) \right]. \quad (12)$$

Let  $\eta_\gamma$  denote the value of  $\eta$  at  $l_\gamma = 1000$  km. Again we find that the dependence of  $\eta_\gamma$  on  $\rho_0$  is only logarithmic. Therefore, all atmospheric effects will depend only weakly on the precise value of density.

The Earth atmosphere is roughly comprised of three layers: the homosphere from 0 – 90 km, the thermosphere starting at 90 km and ranging up to 250 – 400 km depending on solar and geomagnetic activity, as well as the exosphere which begins at the top of thermosphere and extends into space. In the homosphere, winds and turbulence mix all species very well and thus the composition is independent of altitude. In the thermosphere turbulent mixing ceases to be effective and the different species start to diffuse separately. This diffusion is driven by gravitation and thermal gradients. In the exosphere, finally, the mean free path of the lighter atoms like hydrogen becomes large enough such that they can escape to space. In the thermosphere solar energy is absorbed by the photo-dissociation of molecular oxygen. Thus, a sizable amount of free, atomic oxygen appears and our assumption of constant composition fails. However, in terms of electron density, 2 oxygen atoms have the same number of electrons as 1 oxygen molecule, therefore the total mass density is still a very precise indicator of the electron density<sup>11</sup>.

There are no weather phenomena, in the ordinary sense, in the thermosphere, nonetheless its density does depend on various variable factors. This density distribution depends on the energy input from the Sun via extreme ultraviolet light (EUV) and due to direct heating by charged particles from cosmic radiation and solar wind. As a result, the density depends on the amount of solar EUV radiation, which itself depends on geographic latitude, the time of the year and the apparent local solar time. Also the solar activity and geomagnetic activity

---

<sup>11</sup> We verified that this holds to better than 1% in the relevant altitude range.

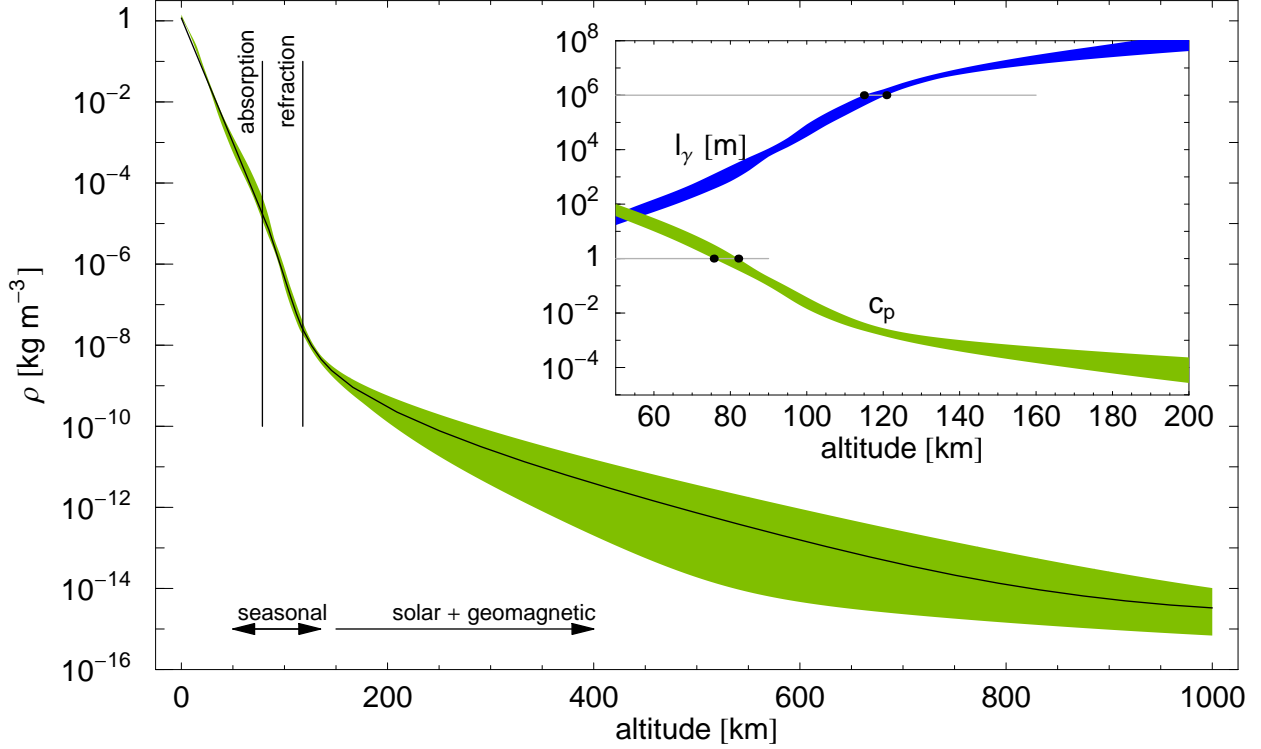


FIG. 3: Total mass density  $\rho$  as function of altitude. The black line shows the default density profile used throughout this paper and corresponds to the medium solar activity case recommended in [28]. The green/gray band denotes the maximal excursions from this default density profile predicted by the NRLMSISE-00 atmospheric model [31]. The inset shows the photon mass induced minimal oscillation length  $l_\gamma$  (blue/dark band) and the absorption coefficient  $c_p$  (green/light band) as functions of the altitude in the relevant range. The bands are due to full variation of density profiles shown in the main plot. The arrows at the bottom denote the main cause for the density variation in that altitude range.

as well as the location within the geomagnetic field do have a non-negligible influence. For a general overview see [28, 32]. Direct measurements of the total mass density in the altitude range from 150 – 200 km can be performed by the observation of the decay rate of very low altitude satellite orbits. These measurements indicate densities of a few times  $10^{-9} \text{ kg m}^{-3}$  at 150 km. The observed diurnal variations are 25%, whereas the observed seasonal variation is somewhat larger with 40% [33, 34].

In [28], the MSISE-90 [35] model<sup>12</sup> is recommended for use in space missions, with three average density profiles from 0 – 900 km corresponding to three different levels of solar and geomagnetic activity. We use the one called medium activity, corresponding to  $F_{10.7} = F_{10.7}^{\text{avg}} = 140$  and  $A_p = 15$ . Where,  $F_{10.7}$  denotes the  $\lambda = 10.7$  cm flux density from the Sun in units of  $10^{-22} \text{ J m}^{-2}$ .  $F_{10.7}^{\text{avg}}$  is the 81 day average of  $F_{10.7}$ . The  $F_{10.7}$  index closely traces the solar UV emissions and the sun spot number.  $A_p$  is the daily average of the  $a_p$  index, which measures the perturbation of the geomagnetic field in units of 2 nT, see section III. The corresponding density profile is shown as black line in figure 3.

In order to study the impact of variations of the density profile we use an updated version of MSISE-90, the so called NRLMSISE-00 [31] model. The differences between the two models for the same set of input parameters, are however small. NRLMSISE-00 takes as input the day of year, the local apparent solar time, the geodetic latitude and longitude,  $F_{10.7}$  and  $F_{10.7}^{\text{avg}}$  and  $A_p$  (or a series of average values of  $A_p$ ). In order to estimate the maximal possible density excursions, we varied:  $F_{10.7}$  and  $F_{10.7}^{\text{avg}}$  jointly from 40 to  $380^{13}$ ,  $A_p$  from 0 to  $100^{14}$ , longitude from  $0^\circ$  to  $90^\circ^{15}$ , the day of the year from 1 to 365, the local apparent solar time from 0 h – 24 h. For each altitude we determined the minimal and maximal value of density due to all these different input parameters, the result is shown as the green/gray band in figure 3. In the altitude range from 50 – 135 km seasonal changes and the geodetic latitude have the greatest effect, whereas for higher altitude the main effects are due solar and geomagnetic activity. These regions are indicated by black arrows in figure 3. The obtained values for density variation agree well with the ones found in [33, 34]. The inset in figure 3 shows how  $\eta_{\text{esc}}$  and  $\eta_\gamma$  change due to those density variations. The values and ranges are:

$$\eta_{\text{esc}} = 78_{-3}^{+4} \text{ km} \quad \text{and} \quad \eta_\gamma = 118 \pm 3 \text{ km}. \quad (13)$$

We see that the limiting factor is indeed refraction and not absorption and both factors need to be included for an accurate calculation. Assuming an axion conversion path of around 1000 km, this is less than a 1% change. We actually verified that the GECOSAX flux does

<sup>12</sup> MSISE stands for 'mass spectrometer and incoherent scatter, extended'.

<sup>13</sup> This covers the extremes during one full 11-year solar cycle, according to [28].

<sup>14</sup> In principle,  $A_p$  can reach values of up to 300 during the strongest geomagnetic storms. These times, would however have to be discarded anyway since the fidelity of geomagnetic model can not be ensured at these times. Note, that the density variations caused by  $A_p > 100$  especially affect the vicinity of 120 km, *i.e.* precisely the regions where  $\eta_\gamma$  will be located.

<sup>15</sup> The  $-90^\circ$  to  $0^\circ$  range just swaps result between summer and winter.

not change by more than 5% due atmospheric density variations, therefore the inclusion of atmospheric effects via an average density profile is fully warranted.

### A. Axion conversion probability

The probability for axion-photon conversion including the full path and medium dependence is given by [17]

$$P_{a\gamma}(m_a, \omega, t) = \mathcal{A}_t \left| \int_0^{\alpha_t} d\lambda' B_{\perp}^{\alpha}(\lambda', t) \cdot \exp \left\{ i \int_0^{\lambda'} d\lambda'' \frac{1}{2} \left[ \frac{m_{\gamma} [h_{P_t}(\lambda'')]^2 - m_a^2}{\omega} - i\Gamma [h_{P_t}(\lambda'')] \right] \right\} \right|^2, \quad (14)$$

with

$$\mathcal{A}_t \equiv \frac{g_{a\gamma}^2}{4} \exp \left\{ - \int_0^{\alpha_t} d\lambda \Gamma [h_{P_t}(\lambda)] \right\} \quad (15)$$

and

$$B_{\perp}^{\alpha}(\lambda', t) \equiv \left| \vec{B} [\vec{p}_t(\lambda')] \times \vec{e}_{\alpha}^t \right|. \quad (16)$$

Here,  $\omega$  is the axion energy. The time dependence of  $P_{a\gamma}$  is entirely due to change of the geometry with time as explained in section II. For each time  $t$  we solve for the position of the satellite  $\vec{X}_t$  and for the position of the Sun  $\vec{S}_t$ . This information is used to derive  $\vec{p}_t(\lambda)$ , the parametric form of the axion path or the line of sight as defined in Eq. 3. The quantity  $\lambda$  parametrizes the position along the line of sight and  $\alpha_t$  denotes the length of the line of sight for the time  $t$ ; we have  $\lambda \in [0, \alpha_t]$ .  $\Gamma$  and  $m_{\gamma}$  only depend on the density of the atmosphere which itself is a functions of the height above mean sea level  $h_{P_t}(\lambda)$ . Only  $\vec{B}$  has a complete dependence on the position vector  $\vec{p}$ . For the various necessary coordinate transformations we refer the reader to appendix A.

The integral in Eq. (14) has no closed form solution and therefore has to be integrated numerically. For the numerical integration a problem arises at very low altitudes, where the air density is high and hence  $m_{\gamma}$  is large. This gives rise to extremely fast oscillation of the integrand of the innermost integral, *i.e.* the integration with respect to  $\lambda''$  becomes practically impossible for sufficiently small heights. On the other hand,  $\Gamma$  also becomes very large and thus those parts of the path where  $m_{\gamma}$  is very large do not contribute to the transition amplitude. The solution is to reverse the direction of integration by substituting  $\lambda$  with  $\alpha_t - \lambda$  and at the same time all integrals now run from  $\alpha_t$  to 0. Next, the integral is partitioned using a simple bisection: First the integral from  $\alpha_t$  to  $\alpha_t/2$  and then from

$\alpha_t/2$  to  $\alpha_t/4 \dots$ , until the contribution of the last part evaluated is smaller than a preset precision goal, in our case this is  $\Delta P/P = 10^{-5}$ .

## B. Solar axion flux

The Sun produces axions throughout its whole interior, although the hottest regions with the highest photon density contribute the bulk of the axion production. Since the angular size of the Sun and the axion producing region are non-negligible compared to the typical angular resolution of x-ray telescopes, we cannot treat the Sun as point source of axions. A detailed study of solar surface axion luminosity has been presented in [13]. Its results have been made accessible to us in machine readable format by one of the authors [36]. We will denote the solar surface axion luminosity by  $\varphi_a(r, E)$ , following the notation in [13], where  $r$  is the dimensionless fraction of the solar radius. Thus, the solar axion flux spectrum produced by the Sun up to a certain radius  $r_s$  is obtained by

$$\left. \frac{d\Phi_\odot}{dE} \right|_{r_s} = 2\pi \int_0^{r_s} dr r \varphi_a(r, E). \quad (17)$$

The usually quoted solar axion flux assumes  $r_s = 1$  and can be written as [13]

$$\left. \frac{d\Phi_\odot}{dE} \right|_{r_s=1} = 6.02 \cdot 10^{10} E^{2.481} \cdot e^{-E/1.205} \left( \frac{g_{a\gamma}}{10^{-10} \text{ GeV}^{-1}} \right)^2 \text{ cm}^{-2} \text{ s}^{-1} \text{ keV}^{-1}. \quad (18)$$

Throughout this work, unless otherwise stated, we use  $g_{a\gamma} = 10^{-10} \text{ GeV}^{-1}$ . Note that the vast majority of this flux originates within the inner 20% of the solar radius, *i.e.*  $r_s = 0.2$ . Since the background will be proportional to  $r_s^2$ , the signal significance will not be optimal for  $r_s = 1$ , but for some smaller value. This issue is studied in detail in appendix B and we adopt  $r_s = 0.13$ . The flux we are using is then given by

$$\frac{d\Phi_\odot}{dE} \equiv \left. \frac{d\Phi_\odot}{dE} \right|_{r_s=0.13} = 1.72 \cdot 10^{10} E^{3.210} \cdot e^{-E/1.135} \left( \frac{g_{a\gamma}}{10^{-10} \text{ GeV}^{-1}} \right)^2 \text{ cm}^{-2} \text{ s}^{-1} \text{ keV}^{-1}. \quad (19)$$

The resulting axion fluence in the energy range from 1 – 10 keV is  $3.58 \cdot 10^{11}$  axions  $\text{cm}^{-2} \text{ s}^{-1}$  for  $r_s = 1$  and it is  $2.21 \cdot 10^{11}$  axions  $\text{cm}^{-2} \text{ s}^{-1}$  for  $r_s = 0.13$ . Also, the mean axion energy changes from 4.2 keV for  $r_s = 1$  to 4.8 keV for  $r_s = 0.13$ . In appendix B, it is demonstrated that the loss of about 40% in signal is compensated by a large decrease in background.

From a comparison of the results obtained in [10] and in [13], it is estimated that this flux calculation is accurate to about 5%, due to changes in the underlying solar model. In our



analysis, we will also neglect the annual variation of the Sun-Earth distance which causes a 5% modulation of the signal.

## V. RESULTING X-RAY FLUXES

### A. General orbits

We now have all the tools at hand to study the GECOSAX effect in detail for any given satellite. Before we delve into finding the optimal orbits in the following section, we briefly describe the GECOSAX flux along a typical orbit. This will help to clarify some notation and to give a basic overview of the issues involved. Figure 4 shows one dark orbit, *i.e.* that part of the orbit which is in the Earth shadow, of satellite 25399 beginning at 2007-12-31, 23:48:33 UTC and lasting 1524 s. We will call the beginning of a dark orbit  $t_d^i$  and the end  $t_d^f$ . The duration of the dark orbit is then given by  $t_d^f - t_d^i$ . Since the satellite may not be able to start observation immediately at  $t_d^i$ , we may have to cut away some time at the beginning and end of the dark orbit, called  $t_{\text{cut}}$ ; thus the useful duration of the orbit is  $t_u = t_d^f - t_d^i - 2t_{\text{cut}}$ . Generally, the duration of dark orbits will vary throughout the year and is different from orbit to orbit. For some parts of the year, there may even be no dark orbits at all, quite analogous to the fact that during summer the Sun does not set north of the polar circle. The integrated useful GECOSAX flux for each dark orbit  $o$ , which corresponds to the blue shaded area in panel (a) of Fig. 4, is given by

$$\langle \Phi \rangle_{\text{gcs}} = \int_{t_d^i + t_{\text{cut}}}^{t_d^f - t_{\text{cut}}} dt' \int_{1 \text{ keV}}^{10 \text{ keV}} dE' P_{a\gamma}(t', E') \frac{d\Phi_{\odot}}{dE}(E'), \quad (20)$$

where  $t_d^{i/f}$  and  $P_{a\gamma}(t', E')$  are different from orbit to orbit and have to be computed correspondingly.

Panel (b) of Fig. 4 shows that the axion conversion path is always considerably longer than the altitude of the satellite, its length ranges from about 1.6 times up to 4 times the altitude of the satellite. This fact is responsible for most of the signal increase with respect to our previous estimate in [15]. Also, within the first and last few 10s of the dark orbit there is large variation in this length: nearly one half of the total path length variation happens within the first and last 60s of the dark orbit. Therefore, in order to be not overly sensitive to errors in timing and positioning we exclude those first and last 60s from the

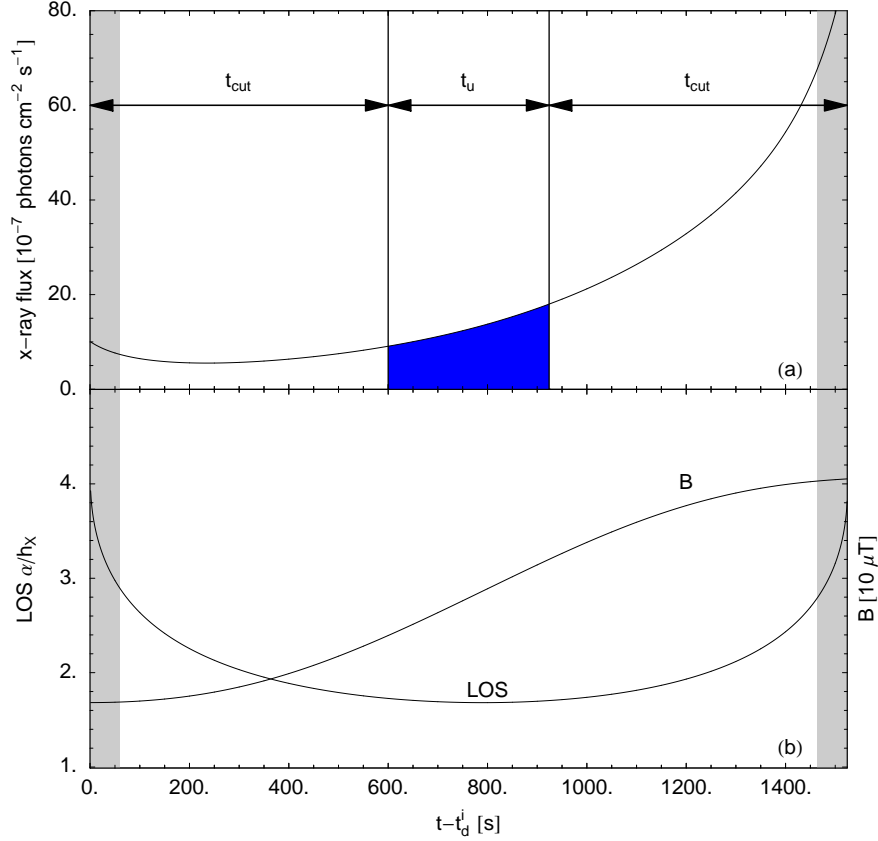


FIG. 4: A typical orbit for satellite 25399.  $t_d^i$  is 2007-12-31, 23:48:33 UTC and the duration of the dark orbit is 1524s. Panel (a) shows the resulting x-ray flux from GECOSAX integrated over the energy range from 1 – 10 keV. The blue shaded area gives the useful integrated GECOSAX flux after accounting for  $t_{\text{cut}}$ . Panel (b) shows the length of the axion conversion path in units of the actual altitude of the satellite (line labeled LOS) and the total magnetic field strength at the location of the satellite B in units of  $10 \mu\text{T}$  (line labeled B). The gray shaded areas are the first and last 60s of the dark orbit.

analysis. This is indicated by the gray shaded areas in Fig. 4. We also see that the variation of the magnetic field is non-negligible. This will depend strongly on the path of the satellite with respect to the geomagnetic field. The orbit of satellite 25399 has an inclination of  $98^\circ$  and thus the satellite does traverse the region of the geomagnetic poles; in this case it is the south geomagnetic pole. Also, Fig. 4 shows that the orientation of the magnetic field is nearly parallel to the axion path at the beginning of the dark orbit since the very large path length right at beginning does not cause a corresponding increase in GECOSAX flux. At the end of the dark orbit the magnetic field has a larger component perpendicular to the

axion path and hence the increase in path length is well reflected in a corresponding increase in the GECOSAX flux.

## B. Optimal orbits

In this section we will apply the formalism developed in the previous sections to determine what constitutes an optimal orbit for observing GECOSAX. In some approximation, the signal is proportional to  $B^2L^2$ , therefore we would like to have orbits which have the maximum possible path length in the highest possible magnetic field. This points to high altitude satellites traversing the region of geomagnetic poles. This requires inclinations greater than about  $70^\circ$ . Instead of designing an optimal orbit, which given the many free parameters is a daunting task, we took a sample of existing orbits, *i.e.* orbits which actually are used or have been used for real scientific satellite missions. We took the TLEs of 50 satellites with apogees below 1000 km from [20]. Nearly, all of these orbits have low eccentricity  $< 0.1$ . The apogees of these satellites have an approximately Gaussian distribution with a mean of 650 km and a standard deviation of about 120 km. The inclinations are strongly clustered around  $80^\circ$ ; 28 satellites have inclinations in the range  $70^\circ - 90^\circ$ . Thus, this sample seems to be well suited for our study. The US SPACECOM identification number and the number of the TLE set used are given in Table III. Our goal here is solely to determine the most suitable orbit and not the most suitable mission, which is the combination of satellite and orbit. Thus, in the following if we speak, say, of satellite 25544<sup>16</sup> we actually just refer to its orbit and not the instruments or the satellite itself.

In determining the optimal orbit we need to distinguish two different observational strategies, called ‘turning mode’ and ‘fixed mode’. A turning mode satellite needs to avoid direct exposure of its x-ray detection system to the sunlight (visible and x-ray) in order to prevent any permanent damage. Typically, this Sun avoidance angle is about  $30^\circ$  and maximum sustained slew rates of  $6^\circ \text{ min}^{-1}$  have been demonstrated. Thus such a satellite enters the Earth shadow pointing  $30^\circ$  away from the Sun, then it needs  $30/6 = 5$  min to turn into observation position pointing to the Sun. Since these numbers may vary from mission to mission and some safety margin will be necessary, we will discard the first 10 minutes at entry into the

---

<sup>16</sup> This is the International Space Station (ISS).

Earth shadow as well as the last 10 minutes prior to exit of the Earth shadow, thus giving up 20 minutes of each orbit. Fixed mode satellites have instrumentation which can withstand direct irradiation by the Sun, or protective shields that can be deployed quickly (compared to slew time), and thus can do their maneuvering to point to the Sun in the bright parts of their orbit. Therefore, in principle, fixed mode satellites can use the entire part of their orbit in the Earth shadow. We have noted previously that the precise time of entry or exit of the Earth shadow are somewhat uncertain due to geometrical and refractive effects. Also the axion conversion rate has its peak values at the entry and exit points where its time derivative is largest. Combining these factors, the GECOSAX rate within first and last few 10s of each dark orbit have fairly high uncertainties. Therefore, we will exclude the first and last 60 seconds of each dark orbit from the analysis even for fixed mode satellites. This is by no means a technical necessity but is a conservative choice to ensure reliability of our results.

For each of the satellites in Table III we computed the integrated, energy averaged GECOSAX flux  $\langle\Phi\rangle_{\text{gcx}}$  for each orbit (about 5500 per satellite) from January 1st 2008 till December 31st 2008 with time steps of 60 s<sup>17</sup>.  $\langle\Phi\rangle_{\text{gcx}}$  is computed in the limit of  $m_a \rightarrow 0$ .  $\langle\Phi\rangle_{\text{gcx}}$  accounts for the time cut away at both ends of the dark orbit; as a result  $\langle\Phi\rangle_{\text{gcx}}$  is different for turning and fixed observation modes. The signal per unit area for a given orbit  $o$  is then given by  $\sigma_o = \langle\Phi\rangle_{\text{gcx}}^o \times t_u^o$ . In reality there will be some background  $b$  as well to the measurement and thus the pertinent quantity to optimize is not the total signal  $s$  but signal divided by the square root of the background  $s/\sqrt{b}$ . We call this quantity significance. The signal is given by  $s_o = \sigma_o \times A$ , where  $A$  is the area of the detector. The background is given by  $b_o = F \times A \times t_u^o$ , where  $F$  is the background rate per unit area.  $F$  here is to be understood as the background rate  $f$  integrated over x-ray energies from  $E_{\text{min}} = 1$  keV to  $E_{\text{max}} = 10$  keV and over the solid angle covered by the axion producing region in the Sun. Assuming a uniform distribution of the background in energy and solid angle, we obtain the following relation  $F = \Omega_s(E_{\text{max}} - E_{\text{min}})f$ . As mentioned in section IV B and explained in detail in appendix B, we take the signal producing region to be  $0.13R_{\odot}$ . The Sun's angular diameter is  $32'$ , thus the solid angle  $\Omega_s$  subtended by the signal producing region is

---

<sup>17</sup>  $t_i^d$  and  $t_f^d$  were determined to within 1 s; '60 s' refers to the integration time step for computing the average flux.

$\Omega_s = \pi(0.13 \cdot 32/2)^2 \text{ arcmin}^2 = 13.6 \text{ arcmin}^2$ . Thus we obtain

$$F = 122.4 \left( \frac{f}{\text{s}^{-1} \text{ cm}^{-2} \text{ keV}^{-1} \text{ arcmin}^{-2}} \right) \text{ s}^{-1} \text{ cm}^{-2}. \quad (21)$$

Next, we define the unit significance for a single orbit  $o$  like this

$$S^o \equiv \frac{t_u^o A \langle \Phi \rangle_{\text{gcx}}^o}{\sqrt{t_u^o A F}} = \underbrace{A^{1/2} F^{-1/2}}_{\equiv Q} \underbrace{t_u^{1/2} \langle \Phi \rangle_{\text{gcx}}^o}_{\equiv \Sigma_o} = Q \Sigma_o. \quad (22)$$

$Q$  is called quality factor and does not depend on a particular orbit but only on the instrument used for x-ray observation<sup>18</sup>, whereas  $\Sigma_o$  is determined by the orbit itself and the observation mode. Using Eq. (21), we can express  $Q$  in terms of  $f$ , which yields

$$Q = 0.09 \text{ cm}^2 \text{ s}^{-1/2} \left( \frac{A}{\text{cm}^2} \right)^{1/2} \left( \frac{\text{s}^{-1} \text{ cm}^{-2} \text{ keV}^{-1} \text{ arcmin}^{-2}}{f} \right)^{1/2}. \quad (23)$$

We now sort all orbits of a particular satellite in decreasing order of  $\Sigma_o$  and add the first  $I$  orbits from the top of the list to the analysis. Thus we can compute the total significance  $S$  for  $I$  orbits:

$$S(I) \equiv \left( \sum_{i=1}^I (S^o)^2 \right)^{1/2} = \left( \sum_{i=1}^I (\Sigma_o Q)^2 \right)^{1/2} = Q \underbrace{\left( \sum_{i=1}^I \Sigma_o^2 \right)^{1/2}}_{\equiv \Sigma} = Q \Sigma \quad \text{with} \quad t_u = \sum_{i=1}^I t_u^i. \quad (24)$$

The maximal possible value for  $I$  is given by the number of orbits in the covered time period, which in our case is one year. The definition of  $S$  is inspired by the form of a Gaussian  $\chi^2$ -function and the fact that for 1 degree of freedom, a  $\chi^2$  difference of  $x$  corresponds to  $\sqrt{x} \sigma$  significance. In this way, the contribution from a particular instrument, encoded in the quality factor  $Q$ , and of a particular orbit, encoded in  $\Sigma$ , can be cleanly separated. The only remaining effect of the particular satellite on  $\Sigma$  is the necessary  $t_{\text{cut}}$ , where fixed and turning mode should bracket most realistic setups.

For each value of  $I$  we obtain a value for  $\Sigma$  and  $t_u$  and we can plot  $\Sigma$  as a function of  $t_u$ . This is shown in Fig. 5 for those 3 satellites which have the largest maximal obtainable  $\Sigma$  in turning (red lines) or fixed mode (blue lines). In case all orbits have a very similar value of  $S_o$ ,  $\Sigma$  is approximately proportional to  $\sqrt{t_u}$ . The fixed mode satellite 25399 exhibits this type of behavior for all times shown in Fig. 5. However, for some satellites (like 13777) all

<sup>18</sup> The background rate  $F$  actually has some dependence on the position relative to the Earth and is not constant in time. We will comment on this point later in more detail.

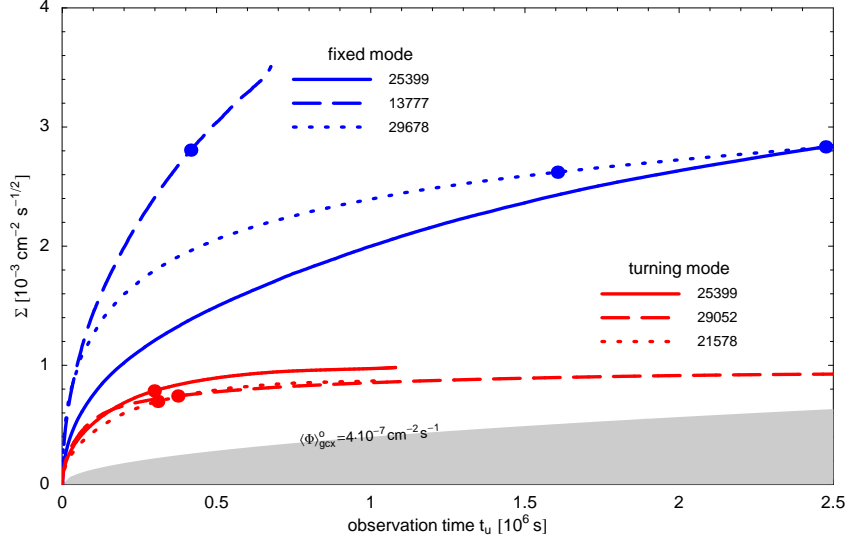


FIG. 5: Shown is the significance  $\Sigma$  as defined in Eq. 24 as a function of the observation time  $t_u$ . In blue those three satellites are shown for which  $\Sigma$  reaches the largest possible value in fixed mode. Whereas, in red the three satellites are shown for which  $\Sigma$  reaches the largest possible value in turning mode. The big dots denote the times at which each satellite has reached 80% of its maximal  $\Sigma$  in the corresponding mode. The gray shaded area shows  $\Sigma$  for the case where the average flux per orbit is constantly  $\langle \Phi \rangle_{\text{gex}}^o = 4 \cdot 10^{-7} \text{ cm}^{-2} \text{ s}^{-1}$ , which corresponds to the result obtained in [15].

available orbits are used up at relatively small values of  $t_u$ . Obviously, satellites which do not have to turn, *i.e.* the fixed mode ones, have a clear advantage. They can accumulate more useful time since they do not lose time by turning once they enter the dark orbit. Moreover, as indicated in Fig. 4, the GECOSAX fluxes are highest either at the very end or beginning of each dark orbit. Thus, they can reach values of  $\Sigma = 0.0035 \text{ cm}^{-2} \text{ s}^{-1/2}$ , about 3 times larger than turning mode satellites. This factor of 3 is very relevant as  $S$  only increases as the square root of time, area or the inverse background rates, therefore a 3 times larger  $\Sigma$  allows a 9 times smaller area or 9 times larger background while having the same statistical significance.

For turning mode satellites (red lines), there are a few long duration, high flux orbits which contribute the bulk to  $\Sigma$  and afterward the curve increases much more slowly than  $\sqrt{t_u}$ . Thus for an optimal use of resources, it is advisable to avoid those orbits and to restrict the axion search to only the best available orbits.

Therefore, we introduce the quantity  $\Sigma_{80} \equiv 0.8\Sigma_{\max}$ , which is just 80% of the maximal obtainable  $\Sigma$ . The reduction in significance is small compared to the savings in observation time when the experiment is restricted to those orbits which allow to reach  $\Sigma_{80}$ .  $\Sigma_{80}$  is marked by a dot on each curve in Fig. 5. The corresponding times  $t_{80}$  are much shorter than the maximal available  $t_u$ ; in case of satellite 29052 the reduction is nearly a factor 10 with a minimal sacrifice in  $\Sigma$ . We see that  $t_{80}$  can be significantly below  $10^6$  s for the best available satellites. For example satellite 13777 in fixed mode would reach a  $\Sigma_{80} = 0.0028 \text{ cm}^{-2} \text{ s}^{-1/2}$  in about 1 week<sup>19</sup>. The values of  $\Sigma_{80}$ , the total time needed and the number of necessary orbits in both fixed and turning mode are listed for all considered satellites in Table III.

All optimal orbits we identified fulfill the naive expectation stated at the beginning of this section: they maximize  $B^2L^2$  by having their dark orbits in the regions of the strongest geomagnetic field and they all have orbits close to the maximum altitude of 1000 km considered here. For the sake of completeness, we have added the performance of the current ISS orbit in Table III. Due to the very low altitude of the ISS of around 380 km, this orbit does not perform very well. On the other hand, if the restriction on the maximal altitude is relaxed, completely new types of orbits become available.

One interesting such class are the so called Molniya orbits, which are highly eccentric with perigees  $\sim 1000$  km and apogees  $\sim 40\,000$  km. These orbits have a period of 12 h and have a repeat ground track, *i.e.* they reach the same point above the Earth every 12 h and can thus cross the geomagnetic pole every second orbit. Due to their primary design goal of allowing communication with high latitudes in Russia, they have their perigee on the Southern hemisphere, some of them very close to geomagnetic South pole. This implies that during antarctic night, which corresponds to the summer months on the northern hemisphere, a satellite on such an orbit would be in darkness in a very high  $B$ -field region at an altitude of  $\sim 1000$  km every 24 h for a duration of about 1 h. Therefore, a few of the best available such orbits out of 24 tested ones are listed as well in Table III. Note that these orbits could reach comparable sensitivities to the best available ones discussed so far. Especially, in turning mode they could yield a significance 20% better than any other orbit. The total observation time needed would be very short, on the order of few  $10^5$  s. However, the variability of the Earth magnetic field so far out is greater and would require a more

---

<sup>19</sup> Including the 2 times 60 s per orbit.

careful consideration than the present note allows for. Also, the obtained bound due to the much longer average length of the axion path, would deteriorate at a smaller value of  $m_a$  compared to the calculation presented in figure 6.

## VI. SENSITIVITY TO $g_{a\gamma}$

In order to compute the sensitivity to  $g_{a\gamma}$  we have to specify a value or range of values for the quality factor  $Q$ . Clearly,  $Q$  is a very instrument-specific quantity and each existing x-ray detector in space will have its unique value of  $Q$ . However, as shown in Eq. (22),  $Q = \sqrt{A/F}$  is a combination of two factors: the effective x-ray collecting area and the background rate  $F$ . In principle, these two factors can be scaled independently. Therefore, we will consider the range of effective areas and range of background rates  $f$  found in real or planned x-ray satellite missions separately. We list the effective area, the background rates ( $f, F$ ) and the resulting quality factor  $Q$  in Table I.

Mission	ID	Instrument	effective area $\text{cm}^2$	background rate $f$ $10^{-8} \text{cm}^{-2} \text{s}^{-1} \text{keV}^{-1} \text{arcmin}^{-2}$	background rate $F$ $10^{-6} \text{cm}^{-2} \text{s}^{-1}$	$Q$ $\text{cm}^2 \text{s}^{1/2}$	reference
XMM <sup>20</sup>	25989	EPIC MOS	900	29	36	5000	[37, 38]
XTE	23757	PCA	7000 <sup>21</sup>	-	3600	2260 <sup>22</sup>	[38, 39]
SUZAKU	28773	XIS FI	250	6.3	7.6	5735	[40] <sup>23</sup>
XEUS <sup>20</sup>	-	-	50000	120	147	18443	[41]

TABLE I: Values for effective area  $A$ , the background rate  $f$  and the integrated background rate  $F$  for various existing and planned x-ray observatories. For those missions already in space we list the US SPACECOM ID number.  $F$  is integrated over the energy range 1–10 keV and the source size of 13.6 arcmin<sup>2</sup>. Given are also the resulting quality factor  $Q$  and the reference for the information.

Table I is not intended to be an exhaustive survey, but to indicate the possibilities of a few contemporary missions. The effective areas range over (250 – 50 000) cm<sup>2</sup>, the background rates  $F$  span  $(8 - 3\,600) \times 10^{-6} \text{cm}^{-2} \text{s}^{-1}$ , and the resulting  $Q$  values are in the range (2 200 –

<sup>20</sup> Not in low Earth orbit.

<sup>21</sup> This number corresponds to the value at the beginning of the mission.

<sup>22</sup> The PCA is a non-imaging detector and hence there is no background rate  $f$  given. Since it covers the whole Sun, the axion flux for  $r_s = 1$  has to be taken, which is 1.6 times larger than the one for  $r_s = 0.13$ . This correction factor has been applied to the  $Q$  value quoted here.

<sup>23</sup> The background cited is the measured value, while observing the dark side of the Earth.



18 000)  $\text{cm}^2 \text{s}^{1/2}$ . Taking the extreme combinations of the effective areas and background rates from this table, the corresponding range of  $Q$  is (300 – 81 100)  $\text{cm}^2 \text{s}^{1/2}$ . For the sensitivity estimate presented in Fig. 6, an effective area of 1 000  $\text{cm}^2$  and a background rate of  $7.6 \times 10^{-6} \text{cm}^{-2} \text{s}^{-1}$  is assumed, yielding  $Q = 11\,471 \text{cm}^2 \text{s}^{1/2}$ . The value  $7.6 \times 10^{-6} \text{cm}^{-2} \text{s}^{-1}$  corresponds to the background rate measured by SUZAKU while observing the dark side of the Earth [40], in the energy range 0.5 – 10 keV. Therefore, this constitutes a guaranteed upper bound on any interfering x-ray luminosity from the dark side of the Earth, *i.e.* down to this level the dark side of the Earth is certainly dark in x-rays. Note that the instruments on board SUZAKU are among the most sensitive ones for extended sources [38].

For the computation of the actual sensitivity to  $g_{a\gamma}$  we will replace the significance defined in Eq. (24) by the correct form of  $\chi^2$ -function. Since the count rates are very low it is necessary to use the Poissonian form of the  $\chi^2$ -function, see *e.g.* [42]. There is considerable variation in the GECOSAX flux along a single dark orbit as is obvious from Fig. 4. Therefore, the signal to noise ratio will also vary greatly and hence this time dependence can be exploited. Thus, the data to be fitted consist of the time series of all time bins of 60 s which are in a dark orbit and are not within  $t_{\text{cut}}$  of either  $t_i^d$  or  $t_f^d$  and belong to one of the those orbits which comprise  $\Sigma_{80}$ .

$$\begin{aligned}
b_{o,i}(E_j) &= F A \Delta t \Delta E, \\
n_{\text{the}}^{o,i}(E_j, m_a) &= g_{10}^4 \langle \Phi_i^o(E_j, m_a) \rangle_{\Delta t, \Delta E} A \Delta t + b_{o,i}(E_j), \\
n_{\text{obs}}^{o,i}(E_j) &= b_{o,i}(E_j),
\end{aligned} \tag{25}$$

with  $g_{10}$  being  $g_{a\gamma}$  in units of  $10^{-10} \text{GeV}^{-1}$ .  $\langle \dots \rangle_{\Delta t, \Delta E}$  is the average over the energy interval  $\Delta E$  and the time interval  $\Delta t$ . Here,  $\Delta E = 1 \text{keV}$  and  $\Delta t = 60 \text{s}$ . Next, we define the  $\chi^2$ -function as follows

$$\chi^2(g_{10}, m_a) = 2 \sum_{o=1}^{o_{80}} \sum_{i=1}^{i_{\Delta t < t_u^o}} \sum_{j=1}^9 n_{\text{the}}^{o,i}(E_j, m_a) - n_{\text{obs}}^{o,i}(E_j) + n_{\text{obs}}^{o,i}(E_j) \ln \frac{n_{\text{obs}}^{o,i}(E_j)}{n_{\text{the}}^{o,i}(E_j, m_a)} \tag{26}$$

The bound  $g_b$  on  $g_{10}$  or  $g_{a\gamma}$  is found by requiring that  $\chi^2(g_b, m_a) = 4$ , thus the bound is at  $2\sigma$  or 95% confidence level. This is repeated for many values of  $m_a$ . The resulting sensitivities for the top performing satellites for both the fixed and the turning mode are shown in Fig. 6 as a function of  $m_a$ . It turns out that accidentally, the same satellite performs best in both modes. The asymptotic sensitivities for  $m_a \rightarrow 0$  are  $4.7 \cdot 10^{-11} \text{GeV}^{-1}$  for fixed mode

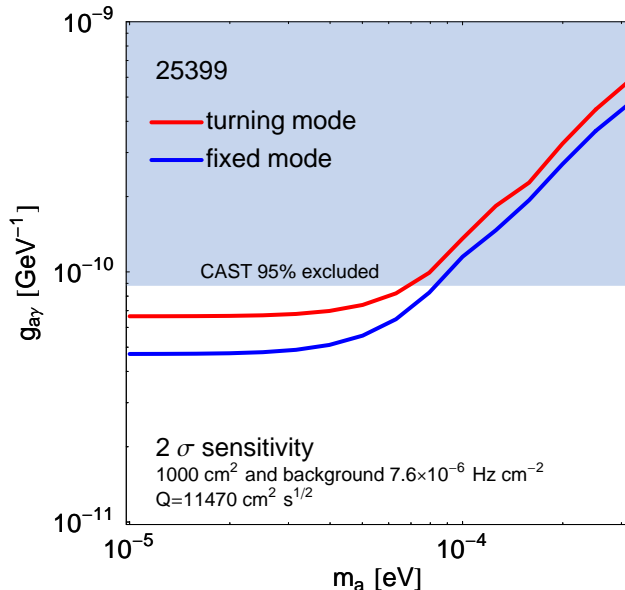


FIG. 6: Sensitivity to  $g_{a\gamma}$  as a function of the axion mass  $m_a$  at  $2\sigma$  (95%) confidence level. The blue shaded region is excluded by the CAST experiment [13].

and  $6.6 \cdot 10^{-11} \text{ GeV}^{-1}$  for turning mode. For comparison the CAST asymptotic bound is  $8.8 \cdot 10^{-11} \text{ GeV}^{-1}$  [13]. Thus a fixed mode observation would improve the CAST limit by about a factor of 2, which is considerable given that the signal scales as  $g_{a\gamma}^4$ , *i.e.* the actual performance in terms of flux sensitivity is more than 12 times better than CAST. Given the fact that the flux sensitivity scales only as square root of time, area and the inverse background rate, the actual increase in time or area would have to be 150-fold to reach this sensitivity.

One important issue for the validity of the result is how it would change if we allow the background to have systematic errors and a time variation. From a purely statistical point of view, we observe that the number of background events per time and energy bin typically is very small with a mean value of  $\mathcal{O}(1)$  for the  $F$  and  $A$  chosen here. Thus the purely statistical variation of the background in each single bin is around 100%, *i.e.* any fully, between all time bins, uncorrelated systematic variation of the background would have to be of that order of magnitude to produce a visible effect. This seems to be very unrealistic. On the other hand, a common mode change of the background, *i.e.* an effective systematic variation of  $F$  would be very difficult to accommodate since the data contains bins with nearly no signal. Those bins severely constrain  $F$ . Therefore, one would have to introduce

a systematic error which closely mimics the time dependence of the axion signal.

Note, however, that almost all time dependence of the background is due to either variations in the geomagnetic field, either by position or due *e.g.* solar wind or due to changes of position with respect to the Sun. Thus, typically, backgrounds will be high if the magnetic field is low. The signal, however, will be large when the magnetic field is high. This is a very strong anti-correlation. Also, the background mostly depends on the total field strength and not on the component perpendicular to the axion path. The position of the satellite with respect to the Sun is not very different for consecutive orbits and hence background events do not mimic the predicted time dependence of the signal. The strongest background rejection, however, is due to the known direction of the signal. Therefore, the same strategy as used by CAST can be applied here as well. The image of the axion-producing core of the Sun in the focal plane of the x-ray telescope will cover only a few pixels out of the whole sensor. All the other pixels can be used to measure the background *in situ*. The main systematics in that case would be due to pointing errors and the width and shape of the point spread function of x-ray optics. In CAST these errors are estimated to be negligible [13].

In comparing the result from a full time and energy binned  $\chi^2$  analysis as defined in Eq. 26 and the one of the simplified treatment using the significance  $\Sigma$  as defined in Eq. 24, we find that using  $\Sigma$  underestimates the flux sensitivity by about 50%. The resulting error in  $g_{a\gamma}$  is about 5%. Thus using  $\Sigma Q$  to estimate the obtainable sensitivity for  $m_a \rightarrow 0$  seems to be a conservative approximation with very reasonable accuracy. Therefore the value of  $\Sigma_{80}$  in Table III can be used for a prediction of the potential of a given satellite or instrument. Using this procedure the sensitivity at  $N\sigma$  can be obtained by

$$\left(\frac{g_b}{10^{-10}\text{GeV}^{-1}}\right) = \left(\frac{\Sigma Q}{N}\right)^{-1/4}. \quad (27)$$

Taking the largest  $Q = 81\,100\text{ cm}^2\text{ s}^{1/2}$  encountered in the discussion of Table I and the largest value of  $\Sigma = 3.5 \times 10^{-3}\text{ cm}^{-2}\text{ s}^{-1/2}$  found from Fig. 5 we get a hypothetical limiting sensitivity of

$$g_b = 2.9 \times 10^{-11}\text{ GeV}^{-1}. \quad (28)$$

## VII. DISCUSSION AND OUTLOOK

The overall accuracy of our GECOSAX flux prediction depends on the accuracy of the geometric description, the magnetic field model, the air density profiles and their effects on x-ray propagation, as well as the numerical implementation of Eq. (14). In section II, we concluded that geometry related effects are accounted for within about  $\pm 25$  km or  $\pm 5$  s. This in turn introduces less than 10% error in the GECOSAX signal prediction. The main sources for these errors are, our purely geometric definition of the Earth shadow and our treatment of TLEs and SGP4. The latter source would be absent in an actual measurement. Also, the time of entry into the Earth shadow is actually easily accessible via the telemetry data of the satellite, *e.g.* electricity production in the solar panels should be a precise indicator. Concerning the magnetic field modeling, we found in section III that B-field errors should be less than 5% resulting in at most a 10% error on the signal. This component may be difficult to improve even in a real experiment. In section IV, we found that a static average atmospheric model can be safely used without introducing more than 5% error on the GECOSAX flux. Numerical integrations and the coordinate transformation should not contribute to the total error budget. We verified our code against available analytical results [17]. We also note that there is an approximately 5% annual modulation of the solar axion flux due to the variation in the Sun-Earth distance. This effect was not accounted for in our computations and modulates our computed signal at the same level. However, this is not a source of uncertainty and is in fact a predicted feature of the signal. Thus, we find that the results for the GECOSAX flux presented here should have an error not exceeding about 15%, which in a real experiment may be reduced down to about 10%. Given the above considerations, low Earth orbit measurements of GECOSAX provide a novel experimental avenue for going beyond the current laboratory bounds on the axion-photon coupling, for axion masses below  $10^{-4}$  eV. We hope that the analysis presented here will help motivate future experimental efforts in this direction.

### Acknowledgments

We would like to thank M. Kuster for collaboration during the early stages of this work as well as comments on a draft version, and D. McCammon for various useful discussions

and the access he provided to the preliminary SUZAKU results. We would also like to thank G. Raffelt for sharing numerical results on solar axion surface luminosity, and S. Maus from NOAA for his clarifications on the WMM 2005. The work of H.D. is supported by the United States Department of Energy under Grant Contract DE-AC02-98CH10886.

- 
- [1] R. D. Peccei and H. R. Quinn, Phys. Rev. Lett. **38**, 1440 (1977).
  - [2] R. D. Peccei and H. R. Quinn, Phys. Rev. **D16**, 1791 (1977).
  - [3] S. Weinberg, Phys. Rev. Lett. **40**, 223 (1978).
  - [4] F. Wilczek, Phys. Rev. Lett. **40**, 279 (1978).
  - [5] J. Preskill, M. B. Wise, and F. Wilczek, Phys. Lett. **B120**, 127 (1983).
  - [6] L. F. Abbott and P. Sikivie, Phys. Lett. **B120**, 133 (1983).
  - [7] M. Dine and W. Fischler, Phys. Lett. **B120**, 137 (1983).
  - [8] M. S. Turner, Phys. Rev. **D33**, 889 (1986).
  - [9] C. Csaki, N. Kaloper, and J. Terning, Phys. Rev. Lett. **88**, 161302 (2002), hep-ph/0111311.
  - [10] G. G. Raffelt, *Stars as Laboratories of Fundamental Physics* (The University of Chicago Press, 1996), 2nd ed.
  - [11] H. Pirmakoff, Phys. Rev. **81**, 899 (1951).
  - [12] P. Sikivie, Phys. Rev. Lett. **51**, 1415 (1983).
  - [13] S. Andriamonje et al. (CAST), JCAP **0704**, 010 (2007), hep-ex/0702006.
  - [14] W. M. Yao et al. (Particle Data Group), J. Phys. **G33**, 1 (2006).
  - [15] H. Davoudiasl and P. Huber, Phys. Rev. Lett. **97**, 141302 (2006), hep-ph/0509293.
  - [16] K. Zioutas, D. J. Thompson, and E. A. Paschos, Phys. Lett. **B443**, 201 (1998), astro-ph/9808113.
  - [17] K. van Bibber, P. M. McIntyre, D. E. Morris, and G. G. Raffelt, Phys. Rev. **D39**, 2089 (1989).
  - [18] J. Meeus, *Astronomical Formulæ for Calculators* (Willmann-Bell, 1988), 4th ed.
  - [19] R. L. R. F. R. Hoots, *Models for propagation of NORAD element sets*, spacetrack report no. 3 ed. (1980).
  - [20] <http://celestrak.com>.
  - [21] <http://www.qsl.net/kd2bd/predict.html>.
  - [22] T. S. Kelso, in *17th AAS/AIAA Space Flight Mechanics Conference* (2007), AAS 07-127.

- [23] <http://www.ngdc.noaa.gov/seg/WMM/soft.shtml>.
- [24] S. McLean, S. Macmillan, S. Maus, V. Lesur, A. Thomson, and D. Dater, Tech. Rep. NOAA Technical Report NESDIS/NGDC-1, NOAA National Geophysical Data Center (2004).
- [25] H. E. Coffey and E. H. Erwin, *Journal of Atmospheric and Solar-Terrestrial Physics* **63**, 551 (2001).
- [26] M. Siebert, *Maßzahlen der erdmagnetischen Aktivität* (Springer, 1971), vol. 49 of *Handbuch der Physik*, pp. 206–275.
- [27] S. Maus, private communication.
- [28] European cooperation for space standardization, Tech. Rep. ECSS-E-10-04A, European Space Agency (2000).
- [29] B. L. Henke, E. M. Gullikson, and J. C. Davis, *Atomic Data and Nuclear Data Tables* **54**, 181 (1993).
- [30] [http://www.cxro.lbl.gov/optical\\_constants/gastrn2.html](http://www.cxro.lbl.gov/optical_constants/gastrn2.html).
- [31] J. M. Picone, A. E. Hedin, D. P. Drob, and A. C. Aikin, *J. Geophys. Res.* **107**, 1468 (2002).
- [32] L. G. Jacchia, SAO Special Report **332** (1971).
- [33] D. G. King-Hele and J. Hingston, *Planet. Space Sci.* **15**, 1883 (1967).
- [34] B. B. Bowman, *Planet. Space Sci.* **23**, 1659 (1975).
- [35] A. E. Hedin, *J. Geophys. Res.* **96**, 1159 (1991).
- [36] G. Raffelt, private communication.
- [37] J. A. Carter and A. M. Read (2007), astro-ph/0701209.
- [38] K. Mitsuda et al., *Publ. Astron. Soc. Jap.* **59**, 1 (2007).
- [39] M. Revnivtsev, M. Gilfanov, R. Sunyaev, K. Jahoda, and C. Markwardt, *Astron. Astrophys.* **411**, 329 (2003), astro-ph/0306569.
- [40] K. Koyama et al., *Publ. Astron. Soc. Jap.* **59**, 23 (2007).
- [41] A. N. Parmar and M. J. L. Turner, Tech. Rep. SA/05.001/AP/cv, ESA (2006).
- [42] S. Eidelman et al. (Particle Data Group), *Phys. Lett.* **B592**, 1 (2004).
- [43] D. Vallado, *Fundamentals of astrodynamics and applications* (El Segundo California, Microcosm, 2001), 2nd ed.
- [44] Tech. Rep. NIMA TR8350.2, National Imagery and Mapping Agency (2000).

## APPENDIX A: COORDINATE SYSTEMS

Unfortunately, the different algorithms and programs used for the calculation use different coordinate systems which sometimes have non-trivial transformation properties. Therefore, a little digression on commonly used coordinate systems is required. All coordinate systems which can serve as quasi-inertial frames are ultimately defined by astronomical observations. The idea is that very distant astronomical objects like quasars allow us to define the orientation of a triad in space which does not change with time. This triad then can be attached to the barycenter of the Earth. We call this the celestial reference system (CRS). Clearly, the CRS is not exactly inertial, but deviations are very small of order  $10^{-8}$  for special relativistic corrections and  $10^{-10}$  for general relativistic corrections [43]. For example, the equations of motion of a satellite around the Earth, or of the Earth around the Sun are valid in the CRS. Observers typically do not float in space but are attached to the surface of the Earth and thus observations will be relative to this surface, which can be used to define the so called terrestrial reference system (TRS), which due to the rotation of the Earth is clearly not an inertial system.

The task is to find the coordinate transformation from CRS to TRS and its inverse, this process is also referred to as coordinate reduction. This problem is, however, very much complicated by obsolete notations stemming from times when the distinction between astrology and astronomy was not always clear. Moreover, many layers of approximations of varying accuracy are present, owing to the difficulty of implementing a full coordinate reduction without powerful enough computers.

Since both the CRS and TRS have the same origin in the barycenter of the Earth<sup>24</sup>, the full transformation can be described by three time-dependent rotations. In reality, these three rotations are often split into four parts, since this makes it easier to derive suitable approximations:

$$\vec{x}_{\text{CRS}} = \mathbf{P}(t)\mathbf{N}(t)\mathbf{R}(t)\mathbf{W}(t)\vec{x}_{\text{TRS}}, \tag{A1}$$

where  $\mathbf{P}(t)$  accounts for the precession and  $\mathbf{N}(t)$  for the nutation of the Earth spin axis.

---

<sup>24</sup> Note, that the International Celestial Reference Frame (ICRF) has its origin at the barycenter of the solar system. All coordinates we use have their origin at the barycenter of the Earth. The transformation between our Earth-centered CRF and the ICRF is a simple translation.

$\mathbf{R}(t)$  describes the rotation of the Earth and  $\mathbf{W}(t)$  the motion or wobble of the spin axis with respect to the surface of the Earth. The precession is caused mainly by the Sun and the Moon pulling at the equatorial bulge of the Earth, this is called the luni-solar precession. Also, there is some precession of the ecliptic due to the influence of the other planets on the Earth orbit around the Sun, called planetary precession. The combined effects move the Earth axis by about  $50''$  per year. This effect was already known to the ancient Greeks and was supposedly discovered by Hipparchos. Nutation is mainly caused by the fact that the Moon's orbit is inclined with respect to the Earth's equator and hence the Moon's pull on the equatorial bulges changes throughout each month. The full theory of nutation is quite complicated since it receives contributions from many sources. The result is as a main period of 18.6 years and an amplitude varying from  $9''$  to  $17''$ .

The Earth rotation is not uniform either and changes *e.g.* due to the friction caused by the tidal bulges. In the simplest case the required rotation angle would be proportional to

$$\omega_{\oplus}t. \tag{A2}$$

Instead of defining a time dependent angular velocity, all violations of this simple relation are absorbed into the definition of time. The relevant time system is UT1 (Universal Time 1) which is based on observed transit times of distant astronomical objects and basically ensures the validity of Eq. A2. UTC (Universal Time Coordinated) is the one on which our daily life is based on. It is adjusted to keep track of UT1 by insertion of leap seconds whenever required and never differs by more than  $\pm 0.9$  s from UT1.

The wobble of the spin axis exists since the Earth is not a rigid body, but has a liquid interior. It is a very difficult effect to predict; fortunately it is a very small effect of only  $0.1''$ .

In all coordinate transformations used throughout this work, we will neglect effects caused by nutation, the difference between UT1 and UTC as well as any polar wobble, therefore our basic transformation reduces to<sup>25</sup>  $\vec{x}_{\text{CRS}} = \mathbf{P}(t)\mathbf{R}(t)\vec{x}_{\text{TRS}}$ . This choice of approximations is mainly guided by the obtainable accuracy of the satellite orbit prediction system used. The errors induced are about  $\pm 1$  s in timing and less than  $30''$  in angle.

---

<sup>25</sup> This choice, in particular, implies that we do not convert TEME as used by SGP4 into a Mean of Date system.



Next we need to define the Terrestrial Reference System (TRS) or geodetic coordinates (GC). Positions on the Earth are commonly measured by latitude, longitude and height above mean sea level. The Earth is not spherically symmetric, but to a very good approximation<sup>26</sup> an oblate ellipsoid, with a flattening of about 1/300. This is caused by the centrifugal force due to the Earth rotation and the fact the Earth is not a rigid but elastic body. There are two consequences from this definition of GC: the vector normal to the Earth surface no longer points back to the center of the Earth and the latitude is now defined as the angle between the normal to the surface and the equator. The satellite propagation routines use the so called World Geodetic System 72 (WGS72), whereas the geomagnetic model is based on WGS84. The difference between these two system is less than 6'' in latitude, less than 1'' in longitude and less than 6 m in height [44]. Therefore we use them interchangeably in coordinate transformations, whereas the satellite propagation routines use WGS72.

With the exception of GC, all other coordinates system are just simple Cartesian or polar coordinate systems which are related by standard transformations. All numerical algorithms follow the description in chapter 3 of [43]. We will therefore give the correspondence of our notation with the one of [43] in Table II.

Symbol	Origin	Fundamental Plane	Principal direction	Use	Notation in [43]
ECI	Earth	Earth equator	Vernal equinox	Main system for numerical calculations	IJK
TRS	Earth	Earth equator	Greenwich meridian	Intermediate step in coordinate conversion	(IJK) <sub>ITRF</sub>
GC	Earth	Earth equator	Greenwich meridian	Input to geomagnetic model	LatLon
TCM	Site	Local horizon	North	Output of geomagnetic model	-
TC	Site	Local horizon	South	Intermediate step in coordinate conversion	SEZ

TABLE II: Coordinate systems used and their corresponding names used in [43]. Note that some coordinate systems used are Cartesian whereas others are polar.

We will use Cartesian Earth centered inertial coordinates (ECI) for all numerical calculations and thus convert all coordinates into ECI first. The motion of the satellite is directly

<sup>26</sup> In reality, the shape of the Earth, the geoid, is defined as being an equipotential surface of its gravitational potential. There is no simple closed analytic form for the geoid. The deviations from the ellipsoid are called undulation of the geoid and are indeed very small  $< 200$  m. Note, that mountains which can be up to  $\sim 10\,000$  m do not play a role in this paper since x-ray propagation ceases at altitudes well above that, thus only the shape of the geopotential iso-surfaces, which determine air density, at heights above about 50 km are relevant.

evaluated in ECI. Also the position of the Sun is directly given in ECI. The Earth magnetic field is specified by its location in geodetic coordinates (GC) and the result is a vector in topocentric coordinates (TCM). The density of the Earth atmosphere is a function of the altitude which is defined in GC. Together with Table II we obtain the following chain of coordinate transformations for the magnetic field  $\vec{B}$ :

$$\vec{x}_{\text{ECI}} \longrightarrow \vec{x}_{\text{TRS}} \longrightarrow \vec{B}_{\text{TCM}} = \vec{B}(\vec{x}_{\text{GC}}) \xrightarrow{\mathbf{R}_3(\pi)} \vec{B}_{\text{TC}} \longrightarrow \vec{B}_{\text{ECI}}, \quad (\text{A3})$$

where only the non-standard transformations are given on top of each arrow, which is a rotation around the 3 or z-axis to get from TCM to TC.

## APPENDIX B: SIGNAL EXTRACTION REGION AND ANGULAR RESOLUTION

The Sun has an average angular diameter of about  $32'$  and the axion producing region is mostly confined to the inner 20-30% of the solar radius. The typical angular resolution of x-ray telescopes ranges from arc seconds to a few arc minutes, therefore the Sun is not a point source of axions. As a result, the “night-side” image of the Sun in x-rays from GECOSAX will cover a finite area in the focal plane of the telescope and it is possible to select a spot radius  $r$  which optimizes the significance  $s/\sqrt{b}$ . Both the signal and the background will be a function of  $r$ , which we take to be a dimensionless fraction of the solar radius. Since axion production is very much concentrated towards the center of the Sun,  $s$  steeply rises for small values of  $r$  and then saturates at  $r \simeq 0.3$ , whereas the background, assuming it is spatially uniform, will rise as  $r^2$ . Thus there should be a maximum in the significance and the radius for which this happens is called  $r_s$ . Assuming perfect spatial resolution of the telescope and no pointing errors, we find  $r_s = 0.13$ . In the following we will rescale all values of  $s/\sqrt{b}$  by the value obtained at  $r_s$  in this case. The rescaled  $s/\sqrt{b}$  as a function of  $r$  is shown as the black line in Fig. 7.

So far we have assumed that the telescope has perfect resolution and that there are no pointing errors. Both errors have the effect that they will blur the image of the Sun and thus the signal density per unit area will decrease, whereas the background density is unaffected. Therefore the significance will decrease relative to the ideal case and at the same time  $r_s$ , the optimal signal extraction radius will increase. We assume the point spread function,

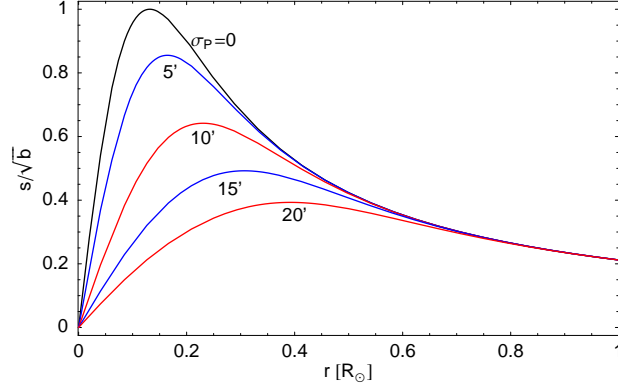


FIG. 7: Relative significance  $s/\sqrt{b}$  as a function of the solar radius. The different curves are for different values of the width of the point spread function as labeled in the plot.

which contains both the effects from pointing errors and the finite optical resolution of the telescope to be a Gaussian with a width or standard deviation of  $\sigma_p$ . The result of finite values for  $\sigma_p$  are shown as blue and red lines in Fig. 7. The values of  $\sigma_p$  next to each line are in arc minutes. The resulting value at maximum is the correction factor which needs to be applied to the product  $\Sigma Q$  in Eq. (27) in order to estimate the limiting sensitivity to  $g_{a\gamma}$ . The SUZAKU telescope has a resolution of better than  $2.5'$  and pointing accuracy of better than  $0.25'$  [38], thus the resulting correction factor is 0.96, which was neglected in computing figure 6.

## APPENDIX C: SATELLITE TLEs AND ORBIT PARAMETERS

TABLE III: This table lists all satellites used throughout this study. Given are the US SPACECOM identification numbers, the name of the satellite and its general orbit parameters. The fixed and turning mode columns show 80% significance  $\Sigma_{80}$  as defined in Eq. 24, the required quality factor to achieve a sensitivity as good as the CAST experiment using  $\Sigma_{80}$ , the number of dark orbits  $n_{80}$  needed to reach  $\Sigma_{80}$ , and the total time needed to achieve  $\Sigma_{80}$  (this includes the contribution of  $t_{\text{cut}}$  for each orbit). The last column for each mode is the corresponding rank within the satellites in this table. '-' indicates that there is no useful dark orbit left after cutting away 600s. TLE set is the number of the TLE set used for the calculations in this paper. All satellite data and TLEs are from [20].

ID	Name	Perigee km	Apogee km	Inclination °	fixed mode					turning mode					TLE set
					$\Sigma_{80}$	$Q_{\text{CAST}}$	$n_{80}$	$t_{80}$	rank	$\Sigma_{80}$	$Q_{\text{CAST}}$	$n_{80}$	$t_{80}$	rank	
					$10^{-3} \text{ cm}^{-2} \text{ s}^{-1/2}$	$10^3 \text{ cm}^2 \text{ s}^{1/2}$	$10^6 \text{ s}$								
13777	IRAS	888	924	80.9	2.8	1.2	588	0.5	2	-	-	-	-	-	404
20322	COBE	874	909	81.1	2.5	1.3	445	0.4	4	-	-	-	-	-	548
20580	HST	561	574	28.6	0.7	5.0	2301	4.6	45	0.3	13.2	1931	3.9	35	70
20638	ROSAT	398	419	53.1	0.6	5.9	1754	3.1	48	0.2	17.1	1170	2.2	38	293
21578	SARA	725	754	81.9	2.5	1.3	2061	2.9	5	0.7	4.8	748	1.2	3	148
21701	UARS	368	475	57.1	0.7	4.8	1441	2.4	44	0.2	14.4	1067	2.0	37	290
22012	SAMPEX	427	493	81.6	0.9	3.6	1472	2.2	40	0.3	11.9	820	1.4	33	525
23547	ORBVIEW 1 (MICROLAB)	705	728	70.1	1.7	1.9	1463	2.5	20	0.6	5.3	783	1.4	8	347
23757	XTE	479	492	23.1	0.4	7.5	2420	5.0	50	0.2	20.2	2090	4.3	40	549
25280	TRACE	567	600	82.2	1.9	1.8	1418	1.5	17	0.5	7.2	807	1.2	17	753
25399	SAFIR 2	814	839	81.6	2.8	1.2	1950	2.7	1	0.8	4.2	717	1.2	1	963
25560	SWAS	605	628	70.0	1.7	1.9	1008	1.3	21	0.5	7.0	785	1.3	14	577
25635	ORSTED	652	869	83.5	1.7	2.0	2248	4.6	24	0.5	6.3	1709	3.5	10	287
25636	SUNSAT	653	879	83.4	1.7	1.9	2205	4.4	19	0.5	6.1	1762	3.5	9	934
25646	WIRE	412	434	82.7	0.6	5.8	2459	5.2	47	0.2	21.4	2083	4.4	41	414
25721	ABRIXAS	504	526	48.6	0.9	3.9	1828	3.2	41	0.3	11.1	1261	2.4	30	221
25735	TERRIERS	493	526	82.7	1.0	3.5	2448	4.9	39	0.3	11.5	2070	4.1	31	354
25791	FUSE	743	765	25.1	1.0	3.2	2254	4.5	37	0.4	8.2	1952	3.9	24	116
25978	CLEMENTINE	610	647	81.8	1.4	2.4	2201	4.2	32	0.4	7.8	1714	3.3	23	271
25994	TERRA	704	730	81.8	1.5	2.2	2307	4.7	29	0.4	7.5	1854	3.8	20	308
26033	ACRIMSAT	680	739	81.9	1.5	2.2	2360	4.8	28	0.5	7.1	2003	4.1	16	309
26546	MEGSAT-1	607	639	64.7	1.5	2.3	1384	2.3	30	0.5	6.9	884	1.6	13	316
26561	HETE-2	560	594	2.0	0.5	6.6	2504	5.3	49	0.2	17.2	2219	4.7	39	231
26702	ODIN	582	611	82.1	1.7	2.0	614	0.7	23	0.3	10.1	285	0.4	28	310

continued on next page

TABLE III: continued

ID	Name	Perigee	Apogee	Inclination	fixed mode					turning mode					TLE set
					$\Sigma_{80}$	$Q_{CAST}$	$n_{80}$	$t_{80}$	rank	$\Sigma_{80}$	$Q_{CAST}$	$n_{80}$	$t_{80}$	rank	
		km	km	°	$10^{-3} \text{ cm}^{-2} \text{ s}^{-1/2}$	$10^3 \text{ cm}^2 \text{ s}^{1/2}$	$10^6 \text{ s}$				$10^{-3} \text{ cm}^{-2} \text{ s}^{-1/2}$	$10^3 \text{ cm}^2 \text{ s}^{1/2}$	$10^6 \text{ s}$		
26998	TIMED	619	643	74.1	1.3	2.5	1552	2.6	33	0.5	7.1	764	1.4	15	943
27370	RHESSI	551	583	38.2	0.8	4.0	2049	3.8	42	0.3	11.0	1638	3.2	29	723
27598	FEDSAT	795	827	81.6	2.1	1.6	2179	4.1	12	0.7	4.9	1687	3.2	4	418
27599	WEOS	792	827	81.5	2.0	1.7	2204	4.3	16	0.6	5.3	1731	3.4	7	436
27600	MICRO LABSAT	791	827	81.5	2.0	1.7	2206	4.3	15	0.6	5.3	1730	3.4	6	411
27640	CORIOLIS	823	866	81.2	2.3	1.4	507	0.4	6	-	-	-	-	-	313
27643	CHIPSAT	573	598	86.0	1.2	2.7	1359	2.2	34	0.4	9.2	903	1.7	27	685
27651	SORCE	612	642	40.1	1.1	3.1	1942	3.5	35	0.4	8.6	1546	2.9	25	531
27783	GALEX	692	698	29.1	1.0	3.4	2217	4.3	38	0.4	8.8	1879	3.7	26	331
27843	MOST	825	847	81.2	2.3	1.4	521	0.4	7	-	-	-	-	-	235
27845	QUAKESAT	826	847	81.2	2.3	1.4	522	0.4	9	-	-	-	-	-	215
27846	AAU CUBESAT	820	846	81.3	2.3	1.4	525	0.4	8	-	-	-	-	-	163
27858	SCISAT 1	643	670	73.9	2.2	1.5	961	1.1	10	0.5	6.7	913	1.5	12	379
27945	KAISTSAT	677	715	81.9	1.6	2.1	2364	4.6	25	0.5	6.5	1993	3.9	11	347
28230	GP-B	644	669	87.8	1.8	1.8	1266	1.6	18	0.4	7.8	973	1.6	22	147
28368	DEMETER	664	690	81.9	1.4	2.3	2301	4.6	31	0.4	7.7	1822	3.7	21	185
28485	SWIFT	583	598	20.7	0.6	5.3	2390	4.9	46	0.2	14.0	2092	4.3	36	935
28773	SUZAKU	559	576	31.5	0.7	4.7	2269	4.5	43	0.3	12.3	1893	3.8	34	675
28939	ASTRO-F (AKARI)	699	733	81.7	2.0	1.6	571	0.5	13	-	-	-	-	-	628
29052	FORMOSAT 3	777	838	72.1	2.1	1.6	1322	2.1	11	0.7	4.5	757	1.3	2	651
29107	CLOUDSAT	704	730	81.8	1.5	2.2	2417	4.9	27	0.5	7.2	1885	3.8	19	602
29108	CALIPSO	704	730	81.8	1.5	2.2	2417	4.9	26	0.5	7.2	1885	3.8	18	587
29479	HINODE (SOLAR-B)	687	709	81.9	2.0	1.7	635	0.6	14	-	-	-	-	-	462
29506	SJ-6D	600	628	82.3	1.7	2.0	685	0.7	22	0.1	26.9	127	0.2	42	495
29678	COROT	901	930	89.2	2.6	1.3	1287	1.8	3	0.6	5.2	1032	1.8	5	376
31304	AIM	586	620	81.8	1.0	3.2	2403	5.1	36	0.3	11.5	2005	4.3	32	275
25544	ISS (ZARYA) <sup>27</sup>	347	365	51.8	0.4	8.9	1741	3.1	-	0.1	26.4	1158	2.2	-	125
21118	MOLNIYA 1-80 <sup>28</sup>	792	39608	63.5	1.9	1.8	79	0.2	-	0.9	3.6	73	0.2	-	434
21196	MOLNIYA 3-40 <sup>28</sup>	721	39664	63.2	1.9	1.8	87	0.2	-	1.0	3.5	84	0.2	-	733
22729	MOLNIYA 3-45 <sup>28</sup>	683	39725	63.8	2.0	1.7	42	0.1	-	0.9	3.8	49	0.1	-	589
23211	MOLNIYA 3-46 <sup>28</sup>	517	39776	62.2	2.0	1.7	31	0.1	-	0.8	4.3	27	0.1	-	347

<sup>27</sup> The ISS orbit is subject to frequent changes due to maneuvering, therefore this result can only serve as a rough indicator of the ISS' orbit quality.

<sup>28</sup> These orbits exceed the validity range of the geomagnetic model and maybe subject to increased uncertainties. To minimize this effect, only those parts of the orbit with altitude below  $1R_{\oplus}$  are considered.